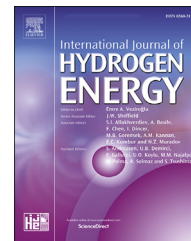


Available online at www.sciencedirect.com

ScienceDirect

journal homepage: www.elsevier.com/locate/hydro

Active and robust novel bilayer photoanode architectures for hydrogen generation via direct non-electric bias induced photo-electrochemical water splitting

Prasad Prakash Patel ^a, Shrinath D. Ghadge ^a,
Prashanth Jampani Hanumantha ^b, Moni Kanchan Datta ^{b,c},
Bharat Gattu ^a, Pavithra Murugavel Shanthi ^a, Prashant N. Kumta ^{a,b,c,d,e,*}

^a Department of Chemical and Petroleum Engineering, Swanson School of Engineering, University of Pittsburgh, Pittsburgh, PA 15261, USA

^b Department of Bioengineering, Swanson School of Engineering, University of Pittsburgh, Pittsburgh, PA 15261, USA

^c Center for Complex Engineered Multifunctional Materials, University of Pittsburgh, PA 15261, USA

^d Mechanical Engineering and Materials Science, Swanson School of Engineering, University of Pittsburgh, Pittsburgh, PA 15261, USA

^e School of Dental Medicine, University of Pittsburgh, PA 15217, USA

ARTICLE INFO

Article history:

Received 20 December 2017

Received in revised form

2 May 2018

Accepted 10 May 2018

Available online 19 June 2018

Keywords:

Photo-electrochemical water splitting

Tin oxide

Tungsten trioxide

Bilayer structure

Nitrogen doping

ABSTRACT

Photo-electrochemical (PEC) water splitting is a promising and environmentally benign approach for generation of hydrogen using solar energy with minimum greenhouse gas emissions. The development of semiconductor materials for photoanode with superior optoelectronic properties combined with excellent photoelectrochemical activity and stability is vital for the realization of viable commercial development of PEC water splitting systems. Herein, we report for the very first time, the study of nanoscale bilayer architecture of WO₃ and Nb and N co-doped SnO₂ nanotubes (NTs), wherein WO₃ NTs are coated with (Sn_{0.95}Nb_{0.05})O₂:N-600 (annealed in NH₃ at 600 °C) layer of different thicknesses, as a potential semiconductor photoanode material for PEC water splitting. An excellent long term photoelectrochemical stability under illumination in the acidic electrolyte solution combined with a solar-to-hydrogen efficiency (STH) of ~3.83% (under zero applied potential) is obtained for the bilayer NTs, which is the highest STH obtained thus far, to the best of our knowledge compared to the other well studied semiconductor materials, such as TiO₂, ZnO and Fe₂O₃. These promising results demonstrate the excellent potential of bilayer NTs as a viable and promising photoanode in PEC water splitting.

© 2018 Hydrogen Energy Publications LLC. Published by Elsevier Ltd. All rights reserved.

* Corresponding author. Department of Bioengineering, 815C Benedum Hall, 3700 O'Hara Street, Pittsburgh, PA 15261, USA.

E-mail address: pkumta@pitt.edu (P.N. Kumta).

<https://doi.org/10.1016/j.ijhydene.2018.05.063>

0360-3199/© 2018 Hydrogen Energy Publications LLC. Published by Elsevier Ltd. All rights reserved.

Introduction

Identification of a sustainable and an economically viable energy supply is the principle and a primary research challenge facing the entire world and the global population today [1–4]. Over the years, the anthropogenic overconsumption of carbonaceous fuels has caused deleterious effects on the environment due to excessive emission of well-known greenhouse gases which are the main drivers contributing to the global climatic change leading to the gradual rise in the earth's temperatures particularly, in the polar ice caps [3–6]. Consequently, the efficient use of energy, transitioning from fossil energy sources into renewable and clean (low carbon footprint) energy sources is of paramount importance to achieve a sustainable energy supply. This will be highly critical in developing a harmonious and energy efficient as well as an energy sufficient modern society meeting the colossal future global demands of an energy intensive technological savvy society with an energy infrastructure that is largely environment-friendly with minimum greenhouse gas emissions [3,4,7–14]. Identification and implementation of these non-carbonaceous energy sources thus, should be efficient, safe, economically producible, and easy to handle with the ability to transport/distribute in a cost-effective manner. In line with the above grave demands, hydrogen has been long considered as a promising clean and non-carbonaceous energy source due to its high energy density (120 MJ/kg for H₂ that is much higher than 44.4 MJ/kg for Gasoline) [15–23]. However, the concomitant progress towards realizing commercialization of hydrogen as a fuel has been largely thwarted due to significant challenges which include economic production, storage and cost-effective distribution of hydrogen [24–27].

Hydrogen production from photoelectrochemical (PEC) splitting of water has received special interest mainly due to the use of non-carbonaceous and environmentally benign implementation of water as a fuel. The absence of greenhouse gas production combined with the lack of any toxic/corrosive byproduct generation in the electrochemical water splitting process makes it an even more attractive approach [25,26]. The utilization of solar energy in driving the water splitting reaction is indeed an attractive option and has gained special interest in recent years, since the sun delivers a massive average energy of 120,000 TW per year to the surface of the Earth [25,28]. Fujishima and Honda's pioneering work on PEC water splitting using n-type TiO₂ semiconductor has clearly demonstrated that PEC water splitting is indeed the foremost technology among the many promising approaches for hydrogen production in an environmentally benign manner [25,29].

The progress of PEC water splitting approach towards commercialization is nevertheless, stymied due to lack of availability of the desired semiconductor materials exhibiting superior light absorption properties, excellent photoelectrochemical activity and stability [25,26]. Materials such as TiO₂, ZnO and α -Fe₂O₃ are widely studied for photoanode applications in PEC water splitting, mainly due to their low cost and ease of availability [21,30–35]. The wide band gap of TiO₂ (~3.2 eV) despite its demonstrated promise, has primarily

limited its use as a photoanode for commercialization of PEC water splitting cells [36–40]. α -Fe₂O₃ on the other hand, faces the major problem related to very short minority carrier (hole) diffusion lengths of the photo-generated carriers, low electron mobility and high recombination rates of the photo-generated carriers [41,42]. In the case of ZnO, inferior light absorption due to the wide band gap (~3.2 eV) and additionally, poor long term stability in aqueous electrolyte solutions are key issues limiting the widespread implementation of ZnO [35,43–45]. On the grounds of different challenges faced by the well-studied semiconductor materials so far as mentioned above, it is clear that identification and development of novel semiconductor materials exhibiting superior optoelectronic properties, excellent photo-electrochemical activity and stability is of paramount importance to realize economic development and consequent commercialization of PEC cells for water splitting.

Amongst the many materials considered to date, SnO₂ is a promising candidate semiconductor material widely explored in dye sensitized solar cells (DSSCs) due to its good electron mobility (~100–200 cm² V⁻¹ s⁻¹ for SnO₂ vs ~10⁻¹ cm² V⁻¹ s⁻¹ for TiO₂) and in addition, it exhibits excellent corrosion resistance in acidic electrolyte solutions [46–49]. However, the wide band gap of SnO₂ (~3.5 eV) offers poor light absorption properties leading to poor photo-electrochemical activity [50]. Systematic band gap engineering was carried out using Nb and N as potential co-dopants for SnO₂ enabling its use for photoanode applications in PEC water splitting and the beneficial results were reported by us earlier [49]. Nb, which is widely used for improving the electrical conductivity of SnO₂ in transparent and conductive oxide thin films (TCO) [51–54], was therefore used as a dopant due to its intrinsic availability of abundant electronic states and more importantly, minor influence on the SnO₂ lattice structure, due to the lower ionic radii of Nb⁴⁺ (69 pm) than Sn⁴⁺ (71 pm) affording good solubility in the solid state [49,55,56].

Nitrogen was also used as a dopant for SnO₂ to achieve hybridization of the substitutional N 2p states with O 2p states and thus, shifting the valence band (i.e., highest occupied molecular orbital, HOMO) upwards, without affecting the conduction band (i.e., lowest unoccupied molecular orbital, LUMO), thereby, reducing the band gap [49,57–61]. Thus, the electronic states of Nb and N simultaneously introduced in the band gap of SnO₂ contributed to significantly reducing the band gap of SnO₂ from ~3.5 eV to ~1.99 eV for (Sn_{0.95}Nb_{0.05})O₂:N-600 nanotubes (NTs) (annealed in NH₃ at 600 °C), resulting in superior light absorption properties as reported by us [49]. These experimental aspects were also ably aided and complemented by the results of theoretical first principles calculations, as reported earlier by us [49]. Nb and N co-doping in SnO₂ as discussed in our earlier report offered 4-orders of magnitude improved carrier density resulting in improved number of carriers available for reaction at the cathode and photoanode [49]. The superior optoelectronic properties of (Sn_{0.95}Nb_{0.05})O₂:N-600 NTs offered improved photoelectrochemical activity with the negative onset potential of (-0.14 V vs RHE) and the highest applied bias photon-to-current efficiency (ABPE) of ~4.1% (at applied potential of -0.75 V vs RHE), which is higher than that obtained using the

other common materials mentioned above namely, ZnO, α -Fe₂O₃ and TiO₂, to the best of our knowledge [35,49,62–65].

In principle, when a semiconductor material is illuminated with light, the photo-generated carriers (electron-hole pairs) recombine very rapidly (~10 ns) [66]. This recombination of photo-generated carriers is a deactivation process, which lowers the number of free carriers available for the reaction at both photoanode and cathode leading unfortunately, to poor photo-electrochemical activity [25,66]. In the case of (Sn_{0.95}Nb_{0.05})O₂:N-600 NTs, it is important to reduce the recombination of the photo-generated carriers and thus, increase the lifetime of photo-generated carriers to improve the photo-electrochemical activity and thus, achieve excellent efficiency with minimum or zero applied potential in addition to solar energy. This can be achieved by coupling (Sn_{0.95}Nb_{0.05})O₂:N-600 NTs with another semiconductor material with suitable band positions. If the conduction band of a semiconductor material is lower than that of (Sn_{0.95}Nb_{0.05})O₂:N-600 NTs, then at the interface of the two semiconductor materials, it is likely that the photo-generated electrons can easily flow from the conduction band of (Sn_{0.95}Nb_{0.05})O₂:N-600 NTs to the conduction band of the other coupled semiconductor material while the holes will remain confined in the (Sn_{0.95}Nb_{0.05})O₂:N-600 NTs, thus resulting in efficient carrier separation providing a long lifetime to the photo-generated carriers as depicted (see Fig. 1a and b) [30,50,66,67]. This will hence, result in more number of photo-generated carriers available for reactions at the cathode and photoanode, leading to efficient hydrogen production from PEC water splitting. In addition, this promising strategy of coupling the two semiconductor materials and generating a bilayer photoanode will offer modified optoelectronic properties due to the redesign and engineering of the band gap at the interface of the two semiconductor materials, while at the same time, contributing to increase in carrier density due to coupling of the two semiconductor materials [30,67,68].

Following this novel strategy, a bilayer photoanode of WO₃ and (Sn_{0.95}Nb_{0.05})O₂:N-600 NTs is created and studied in the present work. The vertical orientation of the nanostructure is chosen as it offers a large area of electrolyte-electrode contact and an efficient path for transport of photo-generated carriers in the material [49,69,70]. Moreover, WO₃ is selected for

coupling with (Sn_{0.95}Nb_{0.05})O₂:N-600 NTs due to its good corrosion resistance in the acidic electrolyte solution combined with superior electron transport properties and positioning of its conduction band at a lower potential than that corresponding to (Sn_{0.95}Nb_{0.05})O₂:N-600 NTs, which is desired due to the reasons mentioned above [49,50,71–74]. This bilayer coupled system corresponding to different thicknesses were accordingly synthesized using ZnO nanowires (NWs) as a sacrificial template employing the ubiquitous hydrothermal method (see Fig. 1b). The photo-electrochemical study was carried out for different thicknesses of the bilayer NTs to study the dependence of the thickness of (Sn_{0.95}Nb_{0.05})O₂:N-600 layer on the carrier lifetime and consequently, on the photo-electrochemical activity of the bilayer NTs.

To the best of our knowledge to date, such a detailed study probing the photo-electrochemical activity of vertically aligned [WO₃-(Sn_{0.95}Nb_{0.05})O₂:N-600] NTs as a bilayer photoanode for PEC water splitting have not been reported. Thus, the present report documents the detailed experimental studies demonstrating the promising photo-electrochemical performance of the novel bilayer composite system, [WO₃-(Sn_{0.95}Nb_{0.05})O₂:N-600] NTs of different thicknesses serving as potentially viable photo-anodes for PEC water splitting. Moreover, the manuscript outlines the efficacy of the composite bilayer system for PEC water splitting without the use of any electrical bias. The report thus, showcases the effectiveness of this novel system to efficiently generate hydrogen directly from PEC water splitting without the use of any electrical bias demonstrating the direct use of solar energy to result in water splitting to generate hydrogen.

Experimental

Synthesis of bilayer photoanode materials

Step 1: Synthesis of sacrificial template-ZnO nanowires (NWs)
Zinc oxide, ZnO nanowires (NWs) were synthesized on fluorine doped tin oxide (FTO) coated glass substrate (0.5 cm × 2.5 cm, Aldrich) using the hydrothermal method, following our earlier published report [35]. The synthesis and characterization of ZnO NWs has also been detailed elsewhere [35].

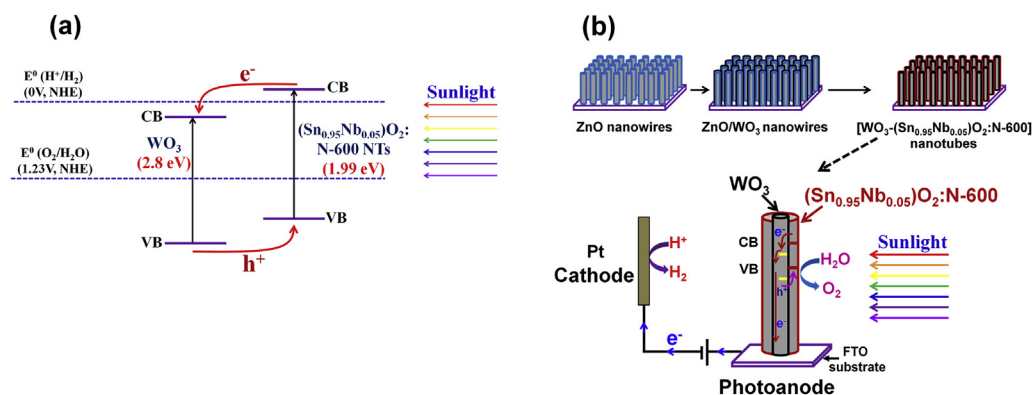


Fig. 1 – (a) Schematic illustration of [WO₃-(Sn_{0.95}Nb_{0.05})O₂:N-600], offering efficient separation of photogenerated carriers, (b) Schematic of the process for synthesizing of bilayer NTs, along with schematic illustration of process of photogenerated electron-hole transfer.

Step 2: Synthesis of ZnO/WO₃ nanowires (NWs)

Tungsten oxide, WO₃ was deposited on ZnO NWs (Fig. 1b) using the wet impregnation method, carried out using ammonium metatungstate (AMT) as the tungsten precursor. The ZnO NWs prepared using the hydrothermal method as outlined above, were dipped in 50 mM AMT solution for ~1 h. The nanowires were then rinsed with D.I. water and dried at 60 °C for 2 h, followed by subsequent heat treatment in air at 500 °C for 30 min to transform the AMT to yield WO₃ [75].

Step 3: Synthesis of bilayer NTs

The synthesized ZnO/WO₃ NWs were then placed in an aqueous solution consisting of 3 mL of 0.15 M ammonium hexafluorostannate (AHFS, Aldrich), stoichiometric amount of ammonium niobate oxalate hydrate (ANOH, Aldrich), 1 mL of 0.5 M boric acid (H₃BO₃, Aldrich) and 1 mL of D.I. water at 26 °C for 30 min. The ensuing hydrolysis of the corresponding precursors resulted in the deposition of (Sn_{0.95}Nb_{0.05})O₂ on ZnO/WO₃ NWs. The acid formed during the hydrolysis process dissolved the sacrificial template (ZnO), resulting in the formation of hollow nanotubes (NTs), denoted as, [WO₃-(Sn_{0.95}Nb_{0.05})O₂]-1 NTs [49,76–78]. After 30 min, the [WO₃-(Sn_{0.95}Nb_{0.05})O₂]-1 NTs were washed with D.I. water and dried at 60 °C for 2 h. Nitrogen incorporation was then carried out by heat treatment of [WO₃-(Sn_{0.95}Nb_{0.05})O₂]-1 NTs for 1 h at 600 °C in anhydrous NH₃ atmosphere (Matheson: 99.99%, flow rate = 100 cm³/min) with ramp rate of 10 °C/min [35,49]. The resultant heat treated material is hereby denoted as bilayer-1 NTs in all of the discussions to follow. A schematic of the synthesis process (mentioned above) is shown in Fig. 1b. The thickness of the (Sn_{0.95}Nb_{0.05})O₂:N-600 layers in bilayer NTs was increased by increasing the concentration of the precursor solutions and then subsequently, following similar synthesis steps as mentioned above. Accordingly, bilayer-2 NTs were synthesized using 3 mL of 0.3 M AHFS solution, stoichiometric amount of ANOH, 1 mL of 1 M H₃BO₃ and 1 mL of D.I. water. Similarly, bilayer-3 NTs were synthesized using 3 mL of 0.45 M AHFS solution, stoichiometric amount of ANOH, 1 mL of 1.5 M H₃BO₃ and 1 mL of D.I. water.

In order to effectively study the effect of coupling of (Sn_{0.95}Nb_{0.05})O₂:N-600 with WO₃ and thus, compare the optoelectronic properties and photoelectrochemical activity of the resultant bilayer photoanode materials with the parent oxide, namely, (Sn_{0.95}Nb_{0.05})O₂:N-600, (Sn_{0.95}Nb_{0.05})O₂:N-600 NTs were synthesized using the synthesis steps reported by us earlier [49]. This involved use of ZnO NWs as the sacrificial template. The synthesized ZnO NWs were then placed in an aqueous solution consisting of 3 mL of 0.15 M AHFS, stoichiometric amount of ANOH, 1 mL of 0.5 M H₃BO₃ and 1 mL of D.I. water at 26 °C for 30 min. After 30 min, (Sn_{0.95}Nb_{0.05})O₂ NTs were washed with D.I. water and dried at 50 °C for 6 h. N doping was carried out by the heat treatment of (Sn_{0.95}Nb_{0.05})O₂ NTs for 1 h at 600 °C in anhydrous NH₃ atmosphere (Matheson: 99.99%, flow rate = 100 cm³/min) with ramp rate of 10 °C/min as previously reported by us [49].

Materials characterization**Structural characterization**

X-ray diffraction. The phase analysis of synthesized materials was carried out by x-ray diffraction (XRD). Accordingly, XRD has been carried out using Philips XPERT PRO system employing CuK_α (λ = 0.15406 nm) radiation at an operating voltage and current of 45 kV and 40 mA, respectively.

Microstructure and optical characterization. The microstructure of the synthesized materials was studied using scanning electron microscopy (SEM). Quantitative elemental analysis was conducted using the energy dispersive x-ray spectroscopy (EDX) analyzer attached to the SEM machine. A Philips XL-30FEG equipped with an EDX detector system comprising an ultrathin beryllium window and Si(Li) detector operating at 20 kV was used for conducting the elemental analysis. Transmission electron microscopy was accordingly conducted using the JEOL JEM-2100F to evaluate the microstructure of the materials used in this study. To study the optical properties, UV–vis absorption spectra of synthesized materials were obtained using the UV–vis spectrophotometer (DU-600, Beckman). All the UV–vis absorption spectra collected were background subtracted.

X-ray photoelectron spectroscopy (XPS). XPS was used to investigate the oxidation states of the various elements in the composite nanotubular photoelectro-catalysts used in the current study. XPS analysis was carried out using the ESCALAB 250 Xi system (Thermo Scientific) equipped with a monochromated Al K_α X-ray source. The standard analysis spot of 400 × 400 μm² was defined by the micro-focused X-ray source. The system is operated at a room temperature in an ultra-high vacuum chamber with the base pressure less than 5 × 10⁻¹⁰ mBar. The binding energy (BE) scale of the analyzer was calibrated to produce <50 meV deviations of the three standard peaks from their standard values. The aliphatic C1s peak was observed at 284.6 eV. High-resolution elemental XPS data in C2p, S2p, Mg2p, and Zn2p regions were acquired with the analyzer pass energy set to 20 eV (corresponding to energy resolution of 0.36 eV) and the step size set to 0.1 eV. The Avantage software package (Thermo Fisher Scientific) was used to fit the elemental spectra based on the calibrated analyzer transmission functions, the Scofield sensitivity factors, and the effective attenuation lengths for photoelectrons from the standard TPP-2M formalism.

Photoelectrochemical characterization

Photoelectrochemical characterization was conducted in 0.5 M H₂SO₄ (electrolyte) solution at 26 °C (temperature of the cell maintained using a Fisher Scientific 910 Isotemp refrigerator circulator) in an electrochemical workstation (VersaSTAT 3, Princeton Applied Research) using a H-type cell, divided into the photoanode and cathode compartments separated by Nafion 115 membrane (Dupont). The photoelectrode was fabricated by fixing a copper wire on the exposed electrically conductive parts of the photoanode

material coated FTO substrates using a silver conductive glue [35,49]. The substrate was sealed properly on all edges with epoxy resin except the active working areas to provide insulation and ensure strong connection [35,49,79]. All the photoelectrochemical measurements were performed using photoelectrode acting as the working electrode (photoanode), Pt wire serving as the counter electrode (cathode) (Alfa Aesar, 0.25 mm thick, 99.95%) and mercury/mercurous sulfate ($\text{Hg}/\text{Hg}_2\text{SO}_4$) electrode (XR-200, Hach) that has a potential of +0.65 V with respect to normal hydrogen electrode serving as the reference. Prior to the photoelectrochemical testing, the test cell was purged with ultra-high purity (UHP-Ar) gas for ~15 min to expel oxygen present in the electrolyte solution. The photoelectrode was illuminated (100 mW cm^{-2}) using a 300 W xenon lamp (Model 6258, Newport) equipped with an AM1.5G filter (Model 81094, Newport) to simulate the solar spectrum and calibrated following the standard manufacturer's instructions.

Linear scan voltammetry

The photoelectrochemical activity of the photoanode materials has been studied by conducting linear scan voltammetry (LSV) using a scan rate of 1 mV s^{-1} under the specific illumination (100 mW cm^{-2}). All reported values of potential in this study are converted to reversible hydrogen electrode using the Nernst equation [35,49]:

$$E_{\text{RHE}} = E_{\text{Hg}/\text{Hg}_2\text{SO}_4} + E_{\text{Hg}/\text{Hg}_2\text{SO}_4}^{\circ} + 0.059\text{pH}$$

E_{RHE} is the potential versus RHE. $E_{\text{Hg}/\text{Hg}_2\text{SO}_4}$ is the potential measured against the $\text{Hg}/\text{Hg}_2\text{SO}_4$ reference electrode. $E_{\text{Hg}/\text{Hg}_2\text{SO}_4}^{\circ}$ is the standard electrode potential of $\text{Hg}/\text{Hg}_2\text{SO}_4$ reference electrode. i_{R_0} corrected linear scan voltammograms (LSVs) after subtracting the current density obtained in the dark, were used for comparison of the photoelectrochemical activity of the different materials.

Electrochemical impedance spectroscopy (EIS)

Electrochemical impedance spectroscopy (EIS) has been carried out for the photoanode materials to determine the charge transfer resistance (R_{ct}) and ohmic resistance (R_{Ω}) [which includes the resistance of various components such as the electrolyte solution (R_{s}) and electrode (R_{e})] [10,12,35,49,80]. EIS has been carried out in the frequency range of 100 mHz–100 kHz (AC Amplitude = 10 mV) at ~0.1 V (vs RHE) using the electrochemical work station (VersaSTAT 3, Princeton Applied Research) under illumination (100 mW cm^{-2}) in 0.5 M H_2SO_4 electrolyte solution. The experimentally obtained EIS plots were fitted using the ZView software from Scribner Associates employing the circuit model $R_{\text{s}}(R_{\text{e}}Q_1)(R_{\text{ct}}Q_{\text{dl}})$, where R_{s} is the solution resistance, R_{e} is the electrode resistance, Q_1 is constant phase element and Q_{dl} represents contribution by double layer capacitance [10,12,35,49,80]. The EIS measurements for the Mott-Schottky plots were performed at frequency of 7.5 kHz with an AC amplitude of 10 mV between the voltage window of –0.8 V to 1.2 V (vs RHE) [35,49,67]. In addition, hall effect measurement was performed with magnetic field strength of 1.02 T (applied perpendicular to the material surface) at room temperature (by Van der Pauw method). Semiconductor samples of

$1 \times 1 \text{ cm}$ in size were used for the Hall effect measurements. Ecopia 3000 system was utilized for Hall measurement. Four gold probes were attached to the corner of the sample and dc current (1 mA) was applied along a diagonal of the square film for the measurement.

Carrier lifetime measurement

To understand the charge transport properties of the bilayer photoanode materials in detail, recombination kinetics of the photo-generated carriers is studied by measuring the open circuit potential as a function of time under light OFF conditions. The decay in the open circuit potential (V_{oc}) as a function of time was studied to gather information about the rate of recombination of the photo-generated carriers in the semiconductor material [30,81]. The decay was calculated from the slope by considering different points in the corresponding rising and saturated segments of the curve, similar to earlier reports [30,67,81–86]. The carrier lifetime (τ), which is the average time for which photo-generated carriers exist before recombining, was determined using the equation [29,84]:

$$\tau = -(k_{\text{B}}T/e)(dV_{\text{oc}}/dt)^{-1}$$

where, k_{B} is Boltzmann constant, T is the absolute temperature (299 K), e is electron charge.

IPCE

To study the effect of light absorption properties on the photoelectrochemical properties, incident photon to current efficiency (IPCE) was determined for bilayer-2 NTs at 0 V and applied bias of 0.6 V (vs RHE) in 0.5 M H_2SO_4 electrolyte solution at 26 °C using different bandpass optical filters with wavelength centered at 350, 400, 450, 500, 550 and 600 nm, similar to earlier reports [49,87–89]. The IPCE is calculated by the equation [89]:

$$\text{IPCE}(\%) = \frac{1240 \times J \times 100}{\lambda \times P}$$

where, J is the measured photocurrent density (mA cm^{-2}), P is the incident light intensity (mW cm^{-2}) at a specific wavelength (λ , nm).

Photoelectrochemical stability test

To study the photoelectrochemical stability of photoanode materials, chronoamperometry (CA) (current density vs time) was performed for 24 h in 0.5 M H_2SO_4 electrolyte solution at 26 °C under illumination (100 mW cm^{-2}), wherein the photoanode material was subjected to a constant potential of ~0.6 V (vs RHE) and the loss in photocurrent density over period of 24 h was analyzed. Additionally, inductively coupled plasma optical emission spectroscopy (ICP-OES, iCAP 6500 duo Thermo Fisher) has been conducted on the electrolyte solution (H_2SO_4) collected after 24 h of CA testing to determine the amount of elements leached out into the solution due to degradation of the photoelectro-catalyst. The amount of elements leached out into the solution from the electrode correspondingly, as is known correlates to the photoelectrochemical stability of the catalyst [10,12,35,49,80]. In order to study the generation of hydrogen from the water splitting reaction directly driven by only solar energy with

zero applied external potential, the photoanode material was illuminated (100 mW cm^{-2}) for 24 h without any external applied potential and the concentration of the evolved gases (at cathode and photoanode) was measured by using a gas chromatograph utilizing helium as the carrier gas (Agilent 7820A).

Results and discussion

Structural characterization

The XRD patterns of $(\text{Sn}_{0.95}\text{Nb}_{0.05})\text{O}_2\text{:N}$ -600 NTs, Bilayer-1 NTs, Bilayer-2 NTs and Bilayer-3 NTs are shown in Fig. 2. The peaks of $(\text{Sn}_{0.95}\text{Nb}_{0.05})\text{O}_2\text{:N}$ -600 NTs (Fig. 2) correspond to that of pure SnO_2 with the tetragonal structure (PDF code: 01-041-1445) [49], displaying no additional peaks corresponding to other Sn and Nb-containing phases indicating co-doping of Nb and N in the SnO_2 lattice, and also no reduction of the FTO substrate due to heat treatment at 600°C similar to that reported earlier and also verified by the UV–Vis absorption spectra of the FTO substrate as discussed later [37,49]. Annealing in NH_3 atmosphere was not performed at temperature higher than 600°C since the reduction of $(\text{Sn}_{0.95}\text{Nb}_{0.05})\text{O}_2$ NTs likely due to the atomic hydrogen originating from the decomposition of NH_3 was observed (at 700°C) as reported earlier as well [37,49]. The XRD patterns of the bilayer materials clearly reveal presence of both WO_3 with the monoclinic structure (PDF code: 01-083-0950) [80] and $(\text{Sn}_{0.95}\text{Nb}_{0.05})\text{O}_2\text{:N}$ -600 NTs with the tetragonal structure (Fig. 2). The lattice parameters of WO_3 – $(\text{Sn}_{0.95}\text{Nb}_{0.05})\text{O}_2\text{:N}$ -600 are slightly lower than that of $(\text{Sn}_{0.95}\text{Nb}_{0.05})\text{O}_2\text{:N}$ -600 (Table S1) suggesting presence of lattice strain due to lattice mismatch between WO_3 and $(\text{Sn}_{0.95}\text{Nb}_{0.05})\text{O}_2\text{:N}$ -600. The lattice parameters decrease from Bilayer-1 NTs to Bilayer-3 NTs (Table S1) suggesting slight lattice contraction, which possibly contributes to the modification in the optoelectronic properties and PEC response as discussed later.

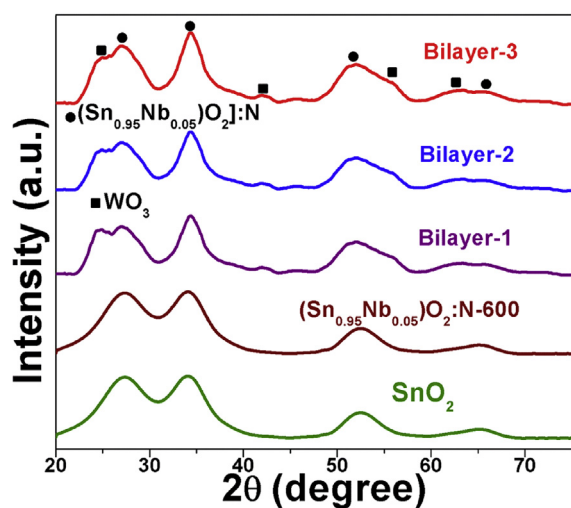


Fig. 2 – The XRD patterns of SnO_2 NTs, $(\text{Sn}_{0.95}\text{Nb}_{0.05})\text{O}_2\text{:N}$ -600 NTs, Bilayer-1 NTs, Bilayer-2 NTs and Bilayer-3 NTs in wide angle 2θ scan.

Scanning electron microscopy (SEM) has been carried out to study the morphology of the representative composition, Bilayer-2 NTs. SEM images showing the top view and cross-sectional view of Bilayer-2 NTs are shown in Fig. 3a. The cross-sectional view of Bilayer-2 NTs shows ~ 12 – $14 \mu\text{m}$ long well-spaced nanotubes. The nanotubes exhibit clean surface with no presence of any particle at the top or at the bottom of the nanotubes. Quantitative elemental analysis of Bilayer-2 NTs has been carried out by energy dispersive x-ray spectroscopy (EDX). The EDX spectrum of Bilayer-2 NTs, shown in Fig. 3a, shows the presence of elements Sn, Nb, W and N. Quantitative elemental composition analysis by EDX of $(\text{Sn}_{0.95}\text{Nb}_{0.05})\text{O}_2\text{:N}$ -600 NTs, Bilayer-1 NTs, Bilayer-2 NTs and Bilayer-3 NTs is shown in Table S1 (Supporting information). The increase in the concentration of Sn, Nb and N combined with the decrease in concentration of W can likely be due to the increase in the thickness of the $(\text{Sn}_{0.95}\text{Nb}_{0.05})\text{O}_2\text{:N}$ -600 NTs layer which is coated on the WO_3 layer.

TEM images of the single and composite bilayer architectures, $(\text{Sn}_{0.95}\text{Nb}_{0.05})\text{O}_2\text{:N}$ -600 NT, Bilayer-1 NT, Bilayer-2 NT and Bilayer-3 NT, displayed in Fig. S1 (Supporting information), reveals clearly the presence of the hollow nanotube with diameter of $\sim 220 \text{ nm}$, $\sim 240 \text{ nm}$, $\sim 270 \text{ nm}$ and $\sim 290 \text{ nm}$, respectively. The larger diameter of Bilayer-1 NT compared to that of $(\text{Sn}_{0.95}\text{Nb}_{0.05})\text{O}_2\text{:N}$ -600 NT can be attributed to the layer of WO_3 on which $(\text{Sn}_{0.95}\text{Nb}_{0.05})\text{O}_2\text{:N}$ -600 layer is coated. The gradual monotonic increase in the diameter of the composite bilayer photoanode materials from Bilayer-1 NT to Bilayer-3 NT is likely due to the increase in the thickness of the $(\text{Sn}_{0.95}\text{Nb}_{0.05})\text{O}_2\text{:N}$ -600 layer due to an increase in the molar concentration of the precursor solutions (AHFS, ANOH and H_3BO_3) used for creating the Nb doped tin oxide NTs, as described in the experimental section of this manuscript (Section Synthesis of bilayer photoanode materials).

The oxidation states of the corresponding elements, Sn, Nb, W and N in the composite bilayer oxide has been determined by performing x-ray photoelectron spectroscopy (XPS) on the respective bilayer composites, Bilayer-1 NTs, Bilayer-2 NTs and Bilayer-3 NTs. The XPS spectrum of Sn (Fig. 3b) of bilayer NTs of different thicknesses shows the presence of Sn $3d_{3/2}$ and $3d_{5/2}$ doublet centered at $\sim 495.27 \text{ eV}$ and $\sim 486.8 \text{ eV}$, corresponding to Sn^{4+} [49,90]. Thus, the negative shift of ~ 0.1 – 0.15 eV is observed in the Sn $3d_{3/2}$ and $3d_{5/2}$ doublets in comparison to that of pure SnO_2 [49]. This can be due to a change in the electron density around the Sn^{4+} ions due to the introduction of Nb and N co-dopants resulting in modification of the electronic structure of SnO_2 (as reported by us earlier) [49,91]. The XPS spectrum of N, shown in Fig. 3c, shows the presence of N 1s peak centered at $\sim 398.3 \text{ eV}$ for Bilayer NTs of different thicknesses indicating the presence of the oxynitride (O–Sn–N or O–Nb–N) and thus resulting in the substitutional doping of N at O sites in the lattice of $(\text{Sn}_{0.95}\text{Nb}_{0.05})\text{O}_2\text{:N}$ NTs as reported earlier [35,37,49,92,93]. The XPS spectrum of Nb shown in Fig. 3d shows the presence of Nb $3d_{3/2}$ and $3d_{5/2}$ doublet centered at ~ 210.3 and ~ 207.5 for $(\text{Sn}_{0.95}\text{Nb}_{0.05})\text{O}_2\text{:N}$ -600 NTs, corresponding to Nb^{4+} , respectively as observed earlier [49,94,95]. Thus, the negative shift of $\sim 0.1 \text{ eV}$ is observed in the Nb $3d_{3/2}$ and $3d_{5/2}$ doublets in comparison to that of NbO_x [96], indicates the presence of oxynitride (O–Nb–N) due to the substitutional doping of N at the O sites in the

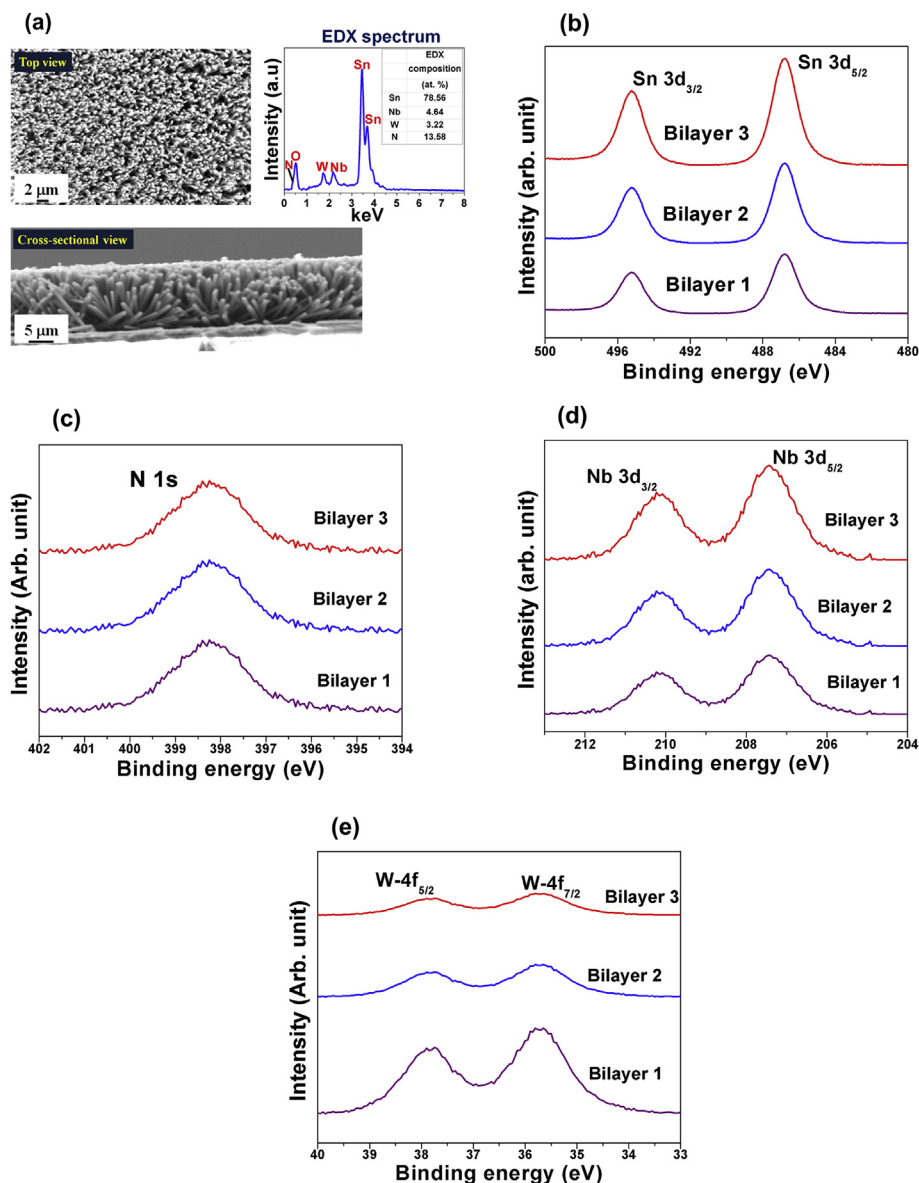


Fig. 3 – (a) SEM micrograph showing top and cross-sectional view along with EDX spectrum of Bilayer-2 NTs, (b) The XPS spectra of bilayer materials showing the Sn 3d_{3/2} and 3d_{5/2} doublets, (c) The XPS spectra of bilayer materials showing the N 1s peak, (d) The XPS spectra of bilayer materials showing Nb 3d_{3/2} and 3d_{5/2} doublets, (e) The XPS spectra of bilayer system showing W 4f_{5/2} and 4f_{7/2} doublet.

composite bilayer which is similar to that reported by us earlier [35,49]. The XPS spectrum of W, shown in Fig. 3e, shows the W 4f_{7/2} and W 4f_{5/2} doublets centered at ~35.7 eV and ~37.9 eV, respectively consistent with bulk WO₃ [80]. The increase in the intensities of the Sn 3d doublets, Nb 3d doublets, N 1s peak along with the corresponding decrease in the intensity of the W 4f doublets is observed as the peak intensities are compared arising from Bilayer-1 NTs to Bilayer-3 NTs bilayer composite samples clearly reflecting the increase in concentration of Sn, Nb and N and decrease in concentration of W on the surface of bilayer photoanode materials, which is likely due to an increase in the thickness of the (Sn_{0.95}Nb_{0.05})

O₂:N-600 NT layer which is coated on the WO₃ NT layer (Fig. S1 in the Supporting information).

Study of the optoelectronic properties

UV–vis absorption study

The light absorption characteristics of the three nanotubular bilayer composite architectures, Bilayer-1 NTs, Bilayer-2 NTs and Bilayer-3 NTs are studied from the UV–vis absorption spectra, shown in Fig. 4a. The UV–vis absorption spectrum of (Sn_{0.95}Nb_{0.05})O₂:N-600 NTs is also shown for comparison in Fig. 4a, in order to study the effect of coupling of the two

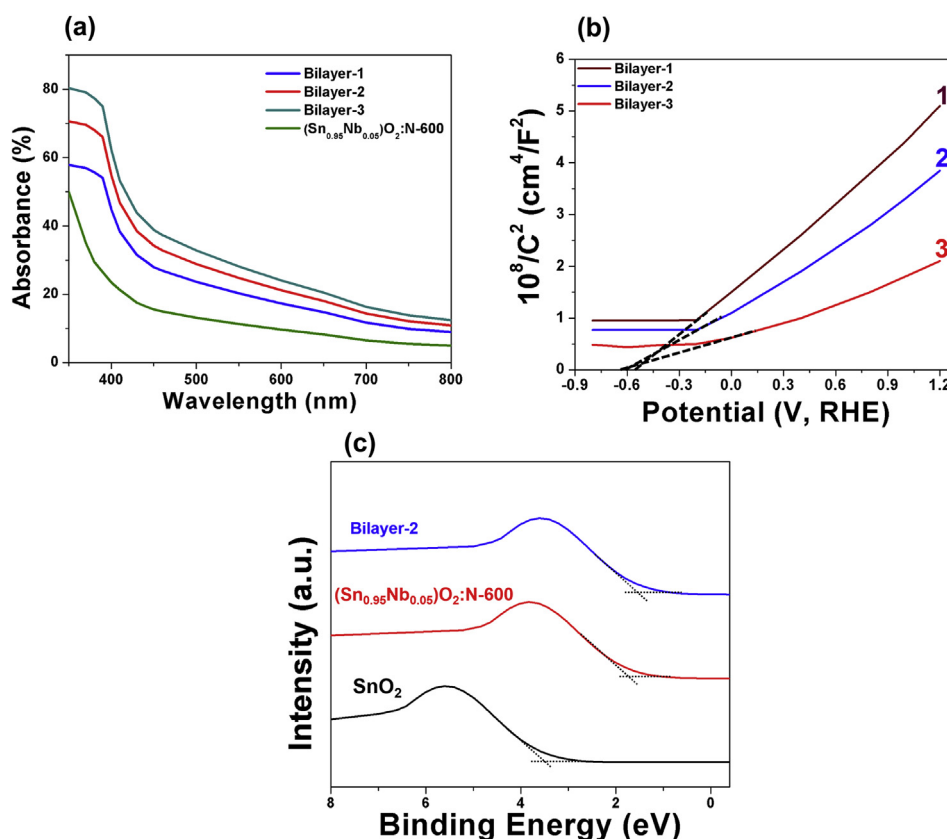


Fig. 4 – (a) UV–vis absorption spectra of $(\text{Sn}_{0.95}\text{Nb}_{0.05})\text{O}_2\text{:N-600}$ NTs, Bilayer-1 NTs, Bilayer-2 NTs and Bilayer-3 NTs, (b) Mott-Schottky plots of Bilayer-1 NTs, Bilayer-2 NTs and Bilayer-3 NTs, (c) Valence band spectra of SnO_2 , $(\text{Sn}_{0.95}\text{Nb}_{0.05})\text{O}_2\text{:N-600}$ and Bilayer-2 NTs.

semiconductor materials, i.e., WO_3 and $(\text{Sn}_{0.95}\text{Nb}_{0.05})\text{O}_2\text{:N-600}$ on the resulting light absorption characteristics. As seen in Fig. 4a, the UV–vis absorption spectrum of $(\text{Sn}_{0.95}\text{Nb}_{0.05})\text{O}_2\text{:N-600}$ NTs show superior light absorption in the visible region indicating red shift in light absorption from the UV region (for pure SnO_2 which is UV active due to wide band gap of ~ 3.5 eV) to the visible region, a consequence of the reduction in the band gap due to Nb and N co-doping in SnO_2 , as reported by us earlier [49]. Also, as mentioned earlier, this can be attributed to electronic states of Nb introduced in the band gap of SnO_2 , along with the appearance of N 2p states at top of the valence band which hybridizes with O 2p states resulting in the shift in the valence band (i.e., highest occupied molecular orbital,

HOMO) upwards, without affecting the conduction band (i.e., lowest unoccupied molecular orbital, LUMO), thereby, reducing the band gap [49,57–61].

The bilayer photoanode materials, i.e., bilayer NTs corresponding to the different thicknesses show superior light absorption characteristics compared to that of the pristine $(\text{Sn}_{0.95}\text{Nb}_{0.05})\text{O}_2\text{:N-600}$ NTs in both the UV and visible regions, suggesting a further reduction in the band gap (Table 1) due to coupling of the WO_3 layer and $(\text{Sn}_{0.95}\text{Nb}_{0.05})\text{O}_2\text{:N-600}$. This can be due to: (I) a redesign of the band gap at the interface of WO_3 and $(\text{Sn}_{0.95}\text{Nb}_{0.05})\text{O}_2\text{:N-600}$ (which are expected to form bilayer structure with staggered type II band alignment) [30,50,68]. The lattice strain is expected to exist at the interface due to a

Table 1 – Results of Mott-Schottky analysis, structural and photoelectrochemical characterization of $(\text{Sn}_{0.95}\text{Nb}_{0.05})\text{O}_2\text{:N-600}$ NTs, Bilayer-1 NTs, Bilayer-2 NTs and Bilayer-3 NTs.

Composition	Carrier density (cm^{-3})	VB edge (eV)	Band gap (eV)	Onset potential (V vs RHE)	Photocurrent density (mA cm^{-2}) at ~ 0.1 V (vs RHE)	R_{ct} ($\Omega \cdot \text{cm}^2$)	ABPE (%) at ~ 0.6 V (vs RHE)	Solar to hydrogen efficiency (STH) (%)
$(\text{Sn}_{0.95}\text{Nb}_{0.05})\text{O}_2\text{:N-600}$ NTs	$4.7 \times (10^{22})$	1.66	1.99	-0.14	0.56	15.3	3.84	–
Bilayer-1 NTs	$4.95 \times (10^{22})$	–	1.95	-0.4	1.93	11.25	4.53	–
Bilayer-2 NTs	$5.6 \times (10^{22})$	1.4	1.93	-0.55	3.1	8.05	5.1	3.83
Bilayer-3 NTs	$6.05 \times (10^{22})$	–	1.9	-0.08	0.35	24.9	3.21	–
FTO	$1.2 \times (10^{20})$	–	–	–	–	–	–	–

lattice mismatch between WO_3 and $(\text{Sn}_{0.95}\text{Nb}_{0.05})\text{O}_2\text{:N-600}$ [30,50,68]. The possible relaxation of the crystal structure can introduce delocalization levels in the band gap resulting in a reduction in the band gap [30,50,68]. (II) a combined effect of both WO_3 (band gap of ~ 2.8 eV) [50] and lower band gap $(\text{Sn}_{0.95}\text{Nb}_{0.05})\text{O}_2\text{:N-600}$ (band gap of ~ 1.99 eV) [49] on the light absorption [67]. Also, it can be seen that the light absorption monotonically increases for the bilayer photoanode materials from Bilayer-1 NTs to Bilayer-3 NTs, which is likely due to the increase in the thickness of the layer of $(\text{Sn}_{0.95}\text{Nb}_{0.05})\text{O}_2\text{:N-600}$ of relatively small band gap (~ 1.99 eV) and superior light absorption properties [49] which is coated on WO_3 layer (having band gap of ~ 2.8 eV [50]) [30,67]. This reduction in the band gap is important, which offers improved light absorption and thus, provides more number of photo-generated carriers to induce the desired reactions at both the cathode and the photoanode, respectively. It is important to note that similar UV–Vis spectra of FTO substrate and FTO substrate annealed at 600°C in NH_3 atmosphere indicate no reduction of substrate (see Fig. S2). The valence band spectra of SnO_2 , $(\text{Sn}_{0.95}\text{Nb}_{0.05})\text{O}_2\text{:N-600}$ and Bilayer-2 NTs were used to study the electronic structure. The top of the valence band measured at the rising edge (Fig. 4c) is ~ 3.5 eV below the Fermi level for pure SnO_2 which is similar to earlier report [97]. The top of the valence band however, shifts to the lower position (~ 1.66 eV) for $(\text{Sn}_{0.95}\text{Nb}_{0.05})\text{O}_2\text{:N-600}$ compared to SnO_2 and further negatively shifts (to ~ 1.4 eV) lower for Bilayer-2 compared to SnO_2 and $(\text{Sn}_{0.95}\text{Nb}_{0.05})\text{O}_2\text{:N-600}$. This negative shift at the top of the valence band to lower potential corresponds well with the decrease in the band gap (as seen in Fig. 4a) and negative shift in V_{FB} (Fig. 4b) also discussed below [67].

Mott-Schottky analysis

The effect of coupling of WO_3 and $(\text{Sn}_{0.95}\text{Nb}_{0.05})\text{O}_2\text{:N-600}$ NTs on the electronic properties is studied following the Mott-Schottky analysis. Following this analysis, the capacitance at the electrode is measured by performing electrochemical impedance spectroscopy (EIS) in the dark in 0.5 M H_2SO_4 electrolyte solution at 26°C . The carrier density for the photoanode material is then determined using the Mott-Schottky equation [35,84]:

$$1/C^2 = (2/e_0\epsilon_0\epsilon\text{N}_d)[(V - V_{\text{FB}}) - kT/e_0] \quad (1)$$

where, e_0 is the electron charge, ϵ is the dielectric constant, ϵ_0 is the permittivity of vacuum, N_d is the carrier density, V is the applied potential, V_{FB} is the flat band potential, k is the Boltzmann constant, T is the absolute temperature (299 K). The Mott-Schottky plot ($1/C^2$ vs V) is plotted for all the three bilayer composite systems namely, for Bilayer-1 NTs, Bilayer-2 NTs and Bilayer-3 NTs and is shown in Fig. 4b. The flat band potential (V_{fb}), determined from the x-intercept of the linear region of the Mott-Schottky plot for Bilayer-1 NTs, Bilayer-2 NTs and Bilayer-3 NTs is $\sim (-0.57$ V vs RHE), $\sim (-0.61$ V vs RHE) and $\sim (-0.63$ V vs RHE), respectively (comparable to that reported earlier [37,67]). Thus, the V_{FB} of Bilayer-1 NTs, Bilayer-2 NTs and Bilayer-3 NTs is more negative than the standard redox potential for water reduction reaction (i.e. hydrogen evolution reaction, HER) (0 V vs NHE), indicative of the more negative position of the conduction band than the standard

redox potential of HER [35,49,67,84]. The decrease in V_{fb} for Bilayer-1 NTs, Bilayer-2 NTs and Bilayer-3 NTs suggests an increase in the shift of the conduction band of the bilayer composite material to higher energy [35,37,49,63,67,84,98–104]. This is expected to result in increase in the driving force for electrons which is important for achieving superior photocurrent density [35,37,63,67,84,98–104]. The V_{fb} of Bilayer-1 NTs, Bilayer-2 NTs and Bilayer-3 NTs is more negative than that of $(\text{Sn}_{0.95}\text{Nb}_{0.05})\text{O}_2\text{:N-600}$ NTs which showed a V_{fb} of $\sim (-0.33$ V) [49] (Fig. S3), indicating that the position of the conduction band of the composite bilayer photoanode materials is at a higher energy than that of $(\text{Sn}_{0.95}\text{Nb}_{0.05})\text{O}_2\text{:N-600}$ NTs [35,37,49,63,67,84,98–104].

The positive slope obtained in the Mott-Schottky plots indicate n-type behavior for $(\text{Sn}_{0.95}\text{Nb}_{0.05})\text{O}_2\text{:N-600}$ NTs, Bilayer-1 NTs, Bilayer-2 NTs and Bilayer-3 NTs. The carrier density is then calculated from the slopes determined from the Mott-Schottky plot using the equation [35,37,49]:

$$\text{N}_d = (2/e_0\epsilon\epsilon_0)[d(1/C^2)/dV]^{-1}$$

The carrier density of the three bilayer composite structures namely, Bilayer-1 NTs, Bilayer-2 NTs and Bilayer-3 NTs is determined to be $\sim 4.95 \times 10^{22}$ cm^{-3} , $\sim 5.6 \times 10^{22}$ cm^{-3} and $\sim 6.05 \times 10^{22}$ cm^{-3} , respectively, which is higher than that of $(\text{Sn}_{0.95}\text{Nb}_{0.05})\text{O}_2\text{:N-600}$ NTs ($\sim 4.7 \times 10^{22}$ cm^{-3}) (Table 1). The carrier density was also measured using the Hall measurement system for three bilayer composites, Bilayer-1 NTs, Bilayer-2 NTs and Bilayer-3 NTs to be $\sim 2.7 \times 10^{22}$ cm^{-3} , $\sim 4.5 \times 10^{22}$ cm^{-3} and $\sim 6.2 \times 10^{22}$ cm^{-3} , respectively, which is also higher than that of $(\text{Sn}_{0.95}\text{Nb}_{0.05})\text{O}_2\text{:N-600}$ NTs ($\sim 1.9 \times 10^{22}$ cm^{-3}).

The higher carrier density of the bilayer photoanode materials contrasted to that of the pristine, $(\text{Sn}_{0.95}\text{Nb}_{0.05})\text{O}_2\text{:N-600}$ NTs can be due to coupling of $(\text{Sn}_{0.95}\text{Nb}_{0.05})\text{O}_2\text{:N-600}$ NTs with the WO_3 resulting in better transfer of electrons from the conduction band of $(\text{Sn}_{0.95}\text{Nb}_{0.05})\text{O}_2\text{:N-600}$ NTs to the conduction band of WO_3 (Fig. 1a and b) leading to a higher density of electrons in WO_3 and thus, resulting in a higher carrier concentration for the bilayer materials similar to that reported earlier [30,84]. Also, the monotonic increase in carrier density measured for Bilayer-1 NTs to Bilayer-3 NTs can be likely due to the systematic increase in the thickness of $(\text{Sn}_{0.95}\text{Nb}_{0.05})\text{O}_2\text{:N-600}$ layer [which exhibits high carrier density ($\sim 4.7 \times 10^{22}$ cm^{-3}) (as reported by us earlier [49]) on the WO_3 layer. It should be noted that the highest carrier density of ($\sim 6.05 \times 10^{22}$ cm^{-3}) obtained in this study for Bilayer-3 NTs is in the range of that of the hydrogen-treated TiO_2 nanowires ($\sim 2.1 \times 10^{22}$ cm^{-3}) [63] which showed excellent photo-electrochemical activity with photo-conversion efficiency of $\sim 1.63\%$ (at applied bias of ~ 0.42 V vs RHE) and WO_3 films with superior photo-electrochemical performance ($\sim 2.5 \times 10^{22}$ cm^{-3}) [105,106]. These results are very important as high carrier density is expected to offer more number of carriers available for the reactions occurring at both the cathode and photoanode, respectively. The increased carrier density for the bilayer photoanode materials from Bilayer-1 NTs to Bilayer-3 NTs is expected to shift the Fermi level upwards towards the conduction band resulting in negative shift in V_{FB} (as discussed earlier) and thus, this is expected to result in increased degree of band bending from Bilayer-1 NTs to Bilayer-3 NTs

[35,37,49,63,84,98–104]. This will offer improved separation of the photo-generated carriers at the interface between the semiconductor material and the electrolyte, leading to improved photo-electrochemical activity [35,37,49,63,84,98–104]. The valence band spectra of SnO_2 , $(\text{Sn}_{0.95}\text{Nb}_{0.05})\text{O}_2\text{:N-600}$ and Bilayer-2 NTs were used to study the electronic structure. The top of the valence band measured at the rising edge (Fig. 4c) is ~ 3.5 eV below the Fermi level for pure SnO_2 which is similar to the published earlier report [97]. The top of the valence band however, shifts to the lower position for $(\text{Sn}_{0.95}\text{Nb}_{0.05})\text{O}_2\text{:N-600}$ compared to SnO_2 and a further negative shift is observed for the composite bilayer structure of Bilayer-2 compared to SnO_2 and $(\text{Sn}_{0.95}\text{Nb}_{0.05})\text{O}_2\text{:N-600}$. This negative shift in the top of the valence band to lower potential corresponds well with the decrease in band gap (as seen in Fig. 4a and Table 1) and negative shift in V_{FB} (Fig. 4b) [67].

Photo-electrochemical characterization

Photo-electrochemical activity

The photo-electrochemical activity of different photoanode materials is studied in 0.5 M H_2SO_4 electrolyte solution. Fig. 5a shows linear scan voltammogram (LSV) curves of $(\text{Sn}_{0.95}\text{Nb}_{0.05})\text{O}_2\text{:N}$ NTs, Bilayer-1 NTs, Bilayer-2 NTs and Bilayer-3 NTs in dark and under illumination of 100 mW cm^{-2} , obtained using scan rate of 1 mV s^{-1} . LSV curves obtained in dark showed a

small current in the range of $\sim 10^{-3} \text{ mA cm}^{-2}$ for all the semiconductor materials. However, under illumination, enhanced photocurrent density is observed for all the semiconductor materials. For $(\text{Sn}_{0.95}\text{Nb}_{0.05})\text{O}_2\text{:N}$ NTs, the onset of photocurrent density begins at $\sim (-0.14 \text{ V vs RHE})$ which is noteworthy as it suggests the need for very minimal external potential in generating the desired photocurrent density from the semiconductor material with superior utilization of the solar energy alone, as reported earlier [49]. The values of the onset potential for all the semiconductor materials studied and presented herein are given in Table 1. The onset of photocurrent density for Bilayer-1 NTs, Bilayer-2 NTs and Bilayer-3 NTs starts at $\sim (-0.4 \text{ V vs RHE})$, $\sim (-0.55 \text{ V vs RHE})$ and $\sim (-0.08 \text{ V vs RHE})$, respectively. The lower onset potential of Bilayer-2 NTs than $(\text{Sn}_{0.95}\text{Nb}_{0.05})\text{O}_2\text{:N}$ NTs and Bilayer-1 NTs indicates superior photo-electrochemical activity of Bilayer-2 NTs than that of $(\text{Sn}_{0.95}\text{Nb}_{0.05})\text{O}_2\text{:N}$ NTs and Bilayer-1 NTs. This can be attributed to: (I) more negative flat band potential and high carrier density (Fig. 4b and Table 1) of Bilayer-2 NTs leading to more negative position of the Fermi level (and thus, conduction band) resulting in more driving force for generating photo-generated electrons [67,84] and (II) efficient separation of the photo-generated carriers with minimum recombination leading to long carrier lifetime (discussed later) for Bilayer-2 NTs [67,84].

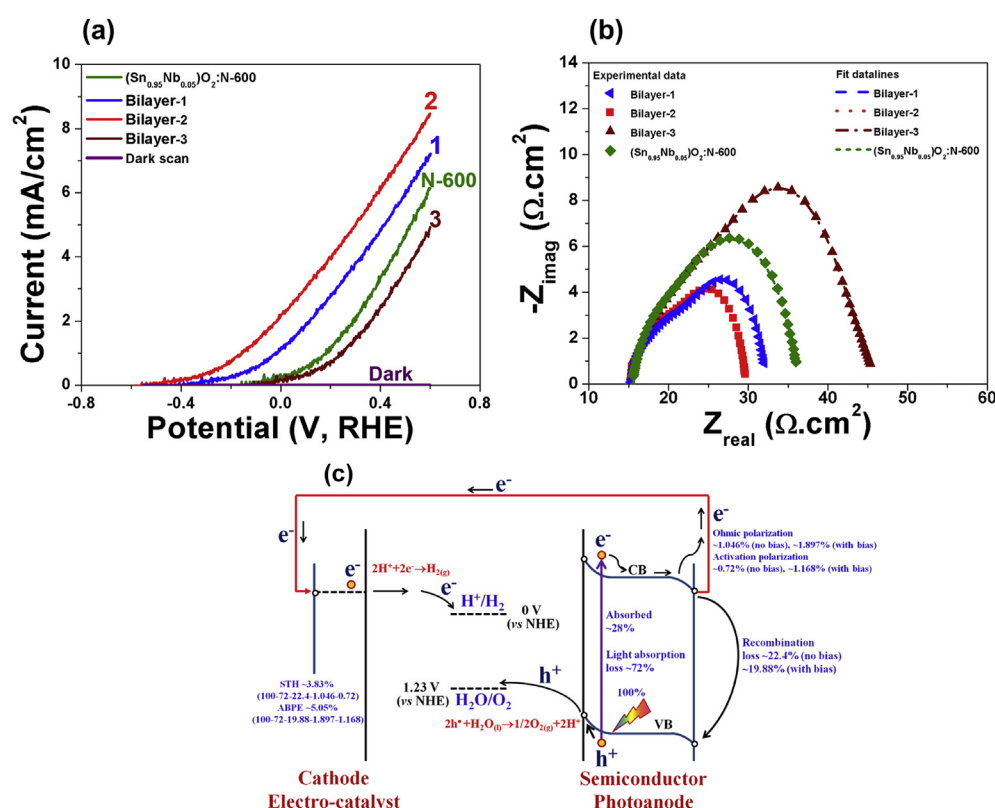


Fig. 5 – (a) The linear scan voltammogram (LSV) curves of $(\text{Sn}_{0.95}\text{Nb}_{0.05})\text{O}_2\text{:N-600}$ NTs, Bilayer-1 NTs, Bilayer-2 NTs and Bilayer-3 NTs in dark and under illumination of 100 mW cm^{-2} measured in 0.5 M H_2SO_4 at 26°C , (b) EIS spectra of $(\text{Sn}_{0.95}\text{Nb}_{0.05})\text{O}_2\text{:N-600}$ NTs, Bilayer-1 NTs, Bilayer-2 NTs and Bilayer-3 NTs obtained at $\sim 0.1 \text{ V}$ (vs RHE) in 0.5 M H_2SO_4 at 26°C in the frequency range of 100 mHz to 100 kHz under illumination (100 mW cm^{-2}), (c) Schematic of the PEC processes showing loss mechanisms without and with -0.6 V bias.

However, the higher onset potential of Bilayer-3 NTs than that of the $(\text{Sn}_{0.95}\text{Nb}_{0.05})\text{O}_2:\text{N}$ NTs, Bilayer-1 NTs and Bilayer-2 NTs suggests poor photo-electrochemical activity for Bilayer-3 NTs which can be due to a higher recombination of the photo-generated carriers resulting in relatively lower carrier lifetime (discussed later). It is noteworthy that the negative onset potential of Bilayer-2 NTs [$\sim(-0.55\text{ V vs RHE})$] suggests that the solar energy alone can be used in generating the desired photocurrent density which is then consumed for generation of hydrogen from water without the need for any external electrical bias or potential. In addition, the more negative onset potential of Bilayer-2 NTs than that of $(\text{Sn}_{0.95}\text{Nb}_{0.05})\text{O}_2:\text{N}$ NTs [$\sim(-0.14\text{ V vs RHE})$] indicates that the bilayer strategy is indeed a promising and effective strategy to improve the photo-electrochemical activity of $(\text{Sn}_{0.95}\text{Nb}_{0.05})\text{O}_2:\text{N}$ NTs. The wide band gap of SnO_2 along with the recombination of the photo-generated carriers usually does not allow for achieving such low onset potentials for PEC water splitting. The tailoring of the band gap of SnO_2 by co-doping with Nb and N and then coupling of the Nb and N co-doped SnO_2 with WO_3 thus, results in this remarkable photo-electrochemical behavior as described herein.

The photocurrent density at a finite potential (to overcome over-potential losses) close to zero bias, i.e., $\sim 0.1\text{ V (vs RHE)}$ in LSV plot (Fig. 5a) is used for comparison of the photo-electrochemical activity of all the semiconductor materials considered in this study. The photocurrent density of $(\text{Sn}_{0.95}\text{Nb}_{0.05})\text{O}_2:\text{N}$ -600 NTs, Bilayer-1 NTs, Bilayer-2 NTs and Bilayer-3 NTs at $\sim 0.1\text{ V (vs RHE)}$ in the LSV plot is $\sim 0.56\text{ mA cm}^{-2}$, $\sim 1.93\text{ mA cm}^{-2}$, $\sim 3.1\text{ mA cm}^{-2}$ and $\sim 0.35\text{ mA cm}^{-2}$ (Table 1). It can be seen that a superior photocurrent density is obtained for Bilayer-1 NTs and Bilayer-2 NTs with the highest current density, obtained for Bilayer-2 NTs (comparable to earlier reports [107,108]) (Table 1) than $(\text{Sn}_{0.95}\text{Nb}_{0.05})\text{O}_2:\text{N}$ NTs, which is mainly due to the improved light absorption properties (see Fig. 4a and Table 1), superior carrier density (Fig. 4b and Table 1), superior reaction kinetics (discussed later) and efficient separation of photo-generated carriers resulting in long carrier lifetime (discussed later). The lower photocurrent density of Bilayer-3 NTs than that of Bilayer-2 NTs can be due to poor reaction kinetics (discussed later) of Bilayer-3 NTs than that of Bilayer-2 NTs despite having higher carrier densities as discussed earlier.

The highest photocurrent density obtained in this study for Bilayer-2 NTs ($\sim 3.1\text{ mA cm}^{-2}$) is ~ 5 fold, ~ 1.55 fold and ~ 8 fold higher than that of $(\text{Sn}_{0.95}\text{Nb}_{0.05})\text{O}_2:\text{N}$ NTs ($\sim 0.56\text{ mA cm}^{-2}$), Bilayer-1 NTs ($\sim 1.93\text{ mA cm}^{-2}$) and Bilayer-3 NTs ($\sim 0.35\text{ mA cm}^{-2}$), respectively. It will be useful to additionally compare the performance of the composite bilayer system in absence of electrical bias in the presence of an electric potential. As is known, the applied bias photon-to-current efficiency (ABPE) for the semiconductor materials is calculated using the equation [35]:

$$\text{ABPE} = I(1.23 - V) \times 100 / J_{\text{light}}$$

wherein, I is the photocurrent density at the measured potential, V is the applied potential and J_{light} is the illumination intensity of 100 mW cm^{-2} . The ABPE is typically evaluated under harsh operating conditions at the applied potential of $\sim 0.6\text{ V (vs}$

RHE, which is the typical potential at which highest ABPE is obtained for semiconductor systems reported date based on TiO_2 , ZnO , Fe_2O_3 , etc. [35,49,62–65]). Under the applied bias, the highest ABPE (at $\sim 0.6\text{ V vs RHE}$) of $\sim 5.1\%$ is obtained for Bilayer-2 NTs which is $\sim 25\%$, $\sim 11.2\%$ and $\sim 38\%$ higher than that of $(\text{Sn}_{0.95}\text{Nb}_{0.05})\text{O}_2:\text{N}$ NTs ($\sim 3.84\%$), Bilayer-1 NTs ($\sim 4.53\%$) and Bilayer-3 NTs ($\sim 3.21\%$), respectively (Table 1). It should be noted that the ABPE of $\sim 5.1\%$ for Bilayer-2 NTs (at $\sim 0.6\text{ V vs RHE}$) is the highest ABPE obtained thus far compared to the other semiconductor materials studied for PEC water splitting based on TiO_2 , ZnO and Fe_2O_3 reported in the open literature to the best of our assessment of the widely reported literature to date [35,49,62–65]. This higher current density and the ABPE achieved is indeed a reflection of the superior electrochemical charge transfer (improved reaction kinetics) characteristics displayed by the bilayer composite architecture, bilayer-2 NTs in comparison to all other materials used in this study.

Electrochemical impedance spectroscopy (EIS) was hence, carried out to determine the charge transfer resistance (R_{ct}) and thus, to study the reaction kinetics for all the materials considered herein in this study. R_{ct} is determined from the diameter of the low frequency semicircle and is tabulated in Table 1. As seen in Fig. 5b, Bilayer-1 NTs ($\sim 11.25\text{ }\Omega\text{ cm}^2$) and Bilayer-2 NTs ($\sim 8.05\text{ }\Omega\text{ cm}^2$) exhibit lower R_{ct} than the pristine $(\text{Sn}_{0.95}\text{Nb}_{0.05})\text{O}_2:\text{N}$ NTs ($\sim 15.3\text{ }\Omega\text{ cm}^2$) and Bilayer-3 NTs ($\sim 24.9\text{ }\Omega\text{ cm}^2$) which is likely due to the efficient separation of the photo-generated carriers with minimum recombination resulting in fast interfacial charge transfer and longer carrier lifetime (discussed later) for the composite bilayer, Bilayer-1 NTs and Bilayer-2 NTs in comparison to $(\text{Sn}_{0.95}\text{Nb}_{0.05})\text{O}_2:\text{N}$ NTs and Bilayer-3 NTs [35,84,109,110].

The lower R_{ct} for Bilayer-2 NTs ($\sim 8.05\text{ }\Omega\text{ cm}^2$) contrasted with Bilayer-1 NTs ($\sim 11.25\text{ }\Omega\text{ cm}^2$) can be due to the more efficient separation and minimum recombination of the photo-generated carriers resulting in longer carrier lifetime (discussed later) for the Bilayer-2 NTs than Bilayer-1 NTs [35,49,84,109,110]. However, Bilayer-3 NTs ($\sim 24.9\text{ }\Omega\text{ cm}^2$) shows higher R_{ct} than Bilayer-1 NTs ($\sim 11.25\text{ }\Omega\text{ cm}^2$), Bilayer-2 NTs ($\sim 8.05\text{ }\Omega\text{ cm}^2$) and $(\text{Sn}_{0.95}\text{Nb}_{0.05})\text{O}_2:\text{N}$ NTs ($\sim 15.3\text{ }\Omega\text{ cm}^2$), which can be due to a higher recombination of the photo-generated carriers resulting in lower carrier lifetime (discussed later) for the composite bilayer, Bilayer-3 NTs than all the other materials described and considered in this study [35,49,84,109,110]. These excellent results show the potential of coupling WO_3 and $(\text{Sn}_{0.95}\text{Nb}_{0.05})\text{O}_2:\text{N}$ -600 in achieving the observed superior photo-electrochemical activity, as evidenced and reported in the results herein.

It is also important to identify the critical losses occurring that limit the attainment of high PEC performance and thus, achieving a high solar to hydrogen (STH) efficiency, which will also aid in choosing a viable approach in engineering novel semiconductor materials in the future (see Section S2 in Supporting Information). In this study, an incident light of 0.1 W cm^{-2} is incident on the bilayer composite heterostructure. An incident photon conversion efficiency (IPCE) of $\sim 20\%$ is obtained for Bilayer-2 NTs (see Section S1 and Fig. S4) at 500 nm (as it is typically the accepted wavelength at which maximum solar irradiance is obtained [111]). Hence, the contribution of energy from the excited carriers for Bilayer-2

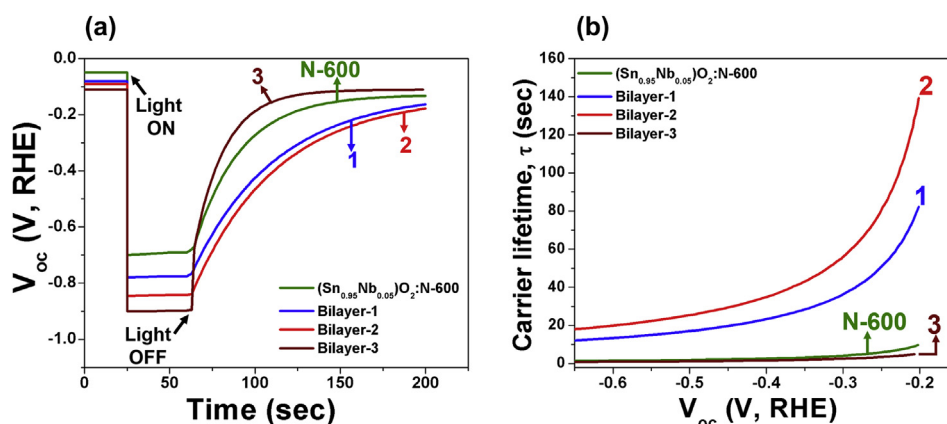


Fig. 6 – (a) Variation of open circuit potential (V_{oc}) under light ON/OFF conditions with time for $(\text{Sn}_{0.95}\text{Nb}_{0.05})\text{O}_2\text{:N-600}$ NTs, Bilayer-1 NTs, Bilayer-2 NTs and Bilayer-3 NTs, (b) Carrier lifetime (τ) as function of open circuit potential (V_{oc}) for $(\text{Sn}_{0.95}\text{Nb}_{0.05})\text{O}_2\text{:N-600}$ NTs, Bilayer-1 NTs, Bilayer-2 NTs and Bilayer-3 NTs.

NTs is $\sim 5.6 \text{ mW cm}^{-2}$ (absorbed light at $\sim 500 \text{ nm} \times \text{IPCE} = 28 \text{ mW cm}^{-2} \times 20\%$) (Fig. 4a, Fig. S4 and Section S1) and thus, the energy that is lost in recombination (absorbed light - IPCE) is $\sim 22.4 \text{ mW cm}^{-2}$ (Section S1). Thus, the contribution of energy from excited carriers is $\sim 5.6\%$ (of incident light intensity, $\sim 100 \text{ mW cm}^{-2}$) and $\sim 22.4\%$ energy is lost in the recombination process. The energy used for overcoming ohmic transfer at photoanode/electrolyte interface (I^2R_{ct}) is $\sim 0.146 \text{ mW cm}^{-2}$ (Section S1). Energy used for overcoming activation polarization at the photoanode/electrolyte interface (I^2R_{ct}) is $\sim 0.077 \text{ mW cm}^{-2}$ (Section S1). Similarly, the energy used for overcoming ohmic transfer at the cathode/electrolyte interface (HER) is $\sim 0.9 \text{ mW cm}^{-2}$ (Section S1). Energy used for activation polarization at cathode/electrolyte interface (HER) is $\sim 0.64 \text{ mW cm}^{-2}$ (Section S1). If overall losses are considered here, $\sim 72\%$ of incident light energy is contributing to light absorption losses at 500 nm (Fig. 4a). Out of $\sim 28\%$ incident light energy absorbed (Fig. 4a), $\sim 5.6 \text{ mW cm}^{-2}$ energy, i.e. with IPCE of 20% , ($\sim 5.6\%$) is available for excited carriers to produce hydrogen gas at the cathode in the PEC cell (Section S1). Remaining $\sim 22.4\%$ absorbed energy is essentially lost in the recombination losses at the defect/trap sites in the bilayer-2 material (Section S1). Out of $\sim 5.6 \text{ mW cm}^{-2}$ energy available for the PEC process, 1.046 mW cm^{-2} is getting lost in ohmic polarization and 0.72 mW cm^{-2} is getting utilized to overcome the activation polarization (i.e., charge transfer) at the electrode/electrolyte interfaces for both cathode and photoanode, respectively (Section S1). The remaining energy ($\sim 3.83 \text{ mW cm}^{-2}$) is thus getting used to convert the incident light energy to hydrogen gas with an efficiency of $\sim 3.83\%$ (Fig. 7b and Section S1).

It should be noted that though the goal is to achieve superior STH at zero applied bias, it is important to study the effect of applied bias on the above mentioned losses which limit the PEC performance. The losses are studied at the applied potential of $\sim 0.6 \text{ V}$ (vs RHE, which is the typical potential at which highest ABPE is obtained for semiconductor systems based on TiO_2 , ZnO , Fe_2O_3 , etc. [35,49,62–65]). Under the applied bias of $\sim 0.6 \text{ V}$, incident energy is $\sim 100 \text{ mW cm}^{-2}$ coming from incident light and $\sim 4.86 \text{ mW cm}^{-2}$ contributed by applied bias (Bias = 0.6 V , $I = \sim 8.1 \text{ mA cm}^{-2}$ shown in Fig. 5a,

Section S2). Thus, the contribution of energy from excited carriers for Bilayer-2 NTs is $\sim 8.11 \text{ mW cm}^{-2}$ [(absorbed light at $\sim 500 \text{ nm} + \text{energy from applied bias}) \times \text{IPCE} = (28 \text{ mW cm}^{-2} + 4.86 \text{ mW cm}^{-2}) \times 24.7\%$] (Fig. 4a and Fig. S4) and thus, the energy that is lost in recombination (absorbed light at $\sim 500 \text{ nm} - \text{energy from excited carriers}$) is $\sim 19.88 \text{ mW cm}^{-2}$. Energy used for overcoming ohmic transfer at photoanode/electrolyte interface (I^2R_{ct}) is $\sim 0.997 \text{ mW cm}^{-2}$ (Section S2). Similarly energy used for overcoming activation polarization at the photoanode/electrolyte interface (I^2R_{ct}) is $\sim 0.528 \text{ mW cm}^{-2}$ (Section S2). The energy used for ohmic transfer at the cathode/electrolyte interface (HER) is $\sim 0.9 \text{ mW cm}^{-2}$ (Section S2). Energy used for activation polarization at cathode/electrolyte interface (HER) is $\sim 0.64 \text{ mW cm}^{-2}$ (Section S2). If overall losses are considered under applied bias, $\sim 72\%$ of incident light energy is contributing to light absorption losses at 500 nm (Fig. 4a). Out of $\sim 28\%$ incident light energy absorbed coupled with input power of 4.86 mW cm^{-2} arising from the applied bias of 0.6 V (Fig. 4a), $\sim 8.12 \text{ mW cm}^{-2}$ energy, considering the IPCE of 24.7% , ($\sim 8.12\%$) is available for the excited carriers to produce hydrogen gas at cathode in the PEC cell (Section S2). Remaining $\sim 19.88\%$ absorbed energy is getting lost in recombination losses in the bilayer-2 material (Section S2). Out of $\sim 8.12 \text{ mW cm}^{-2}$ energy available for PEC process, 1.897 mW cm^{-2} is getting lost in ohmic polarization and 1.168 mW cm^{-2} is getting utilized to overcome activation polarization (i.e., charge transfer) at the electrode/electrolyte interfaces at cathode and photoanode (Section S2). Remaining energy ($\sim 5.1 \text{ mW cm}^{-2}$) is thus getting used to convert incident light energy to hydrogen gas with an efficiency of $\sim 5.1\%$ (Table 1 and Section S2). The recombination losses decrease by a commendable $\sim 12\%$ under applied bias compared to the case with no applied bias for bilayer-2 system, suggesting the promise of bilayer-2 system. The study also suggest that possible further electronic structural modification in the bilayer-2 system configuration could likely minimize the losses with no electrical bias further offering excellent PEC response. Fig. 5c shows a schematic summarizing the various processes outlined above.

It is important to decrease the light absorption losses ($\sim 72\%$), the recombination losses ($\sim 22.4\%$ at zero bias and

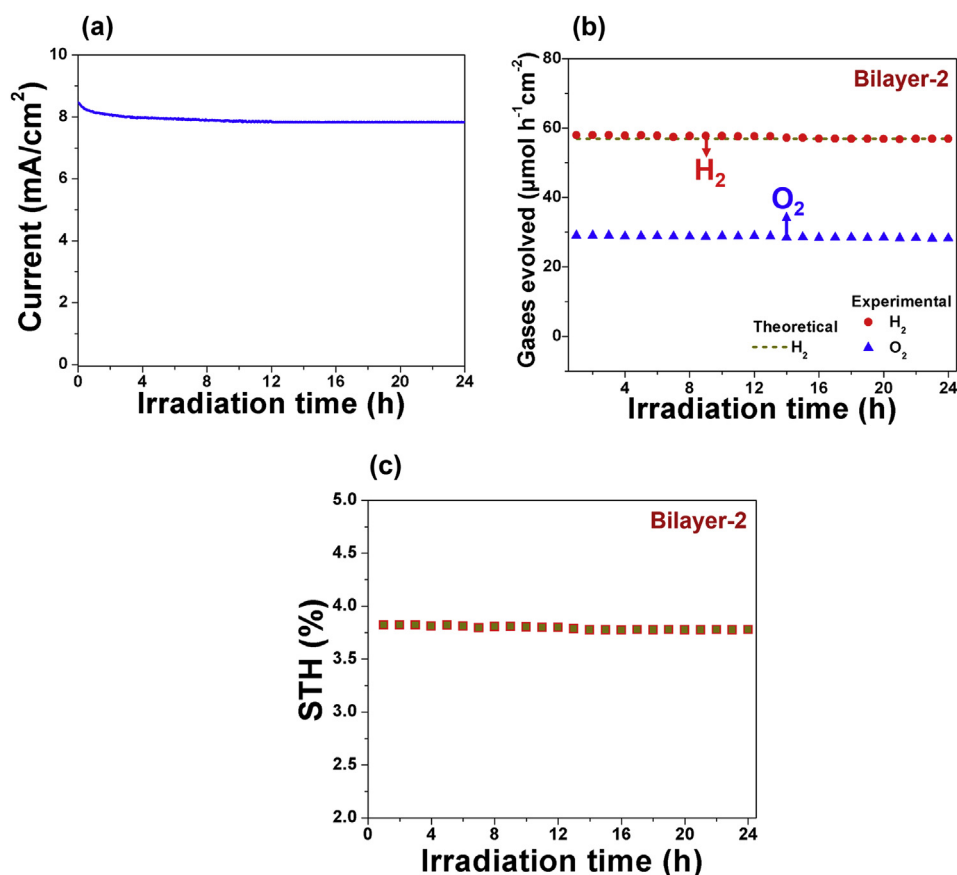


Fig. 7 – (a) The variation of photocurrent density vs irradiation time in the chronoamperometry test of Bilayer-2 NTs, performed in 0.5 M H₂SO₄ solution under a constant potential of ~ 0.6 V (vs RHE) at 26 °C for 24 h under illumination (100 mW cm⁻²), (b) Theoretical and experimentally measured concentration of H₂ gas and experimentally measured concentration of O₂ gas measured under illumination (100 mW cm⁻²) with no applied potential for Bilayer-2 NTs measured in 0.5 M H₂SO₄ solution at 26 °C for 24 h, (c) Variation of solar-to-hydrogen efficiency (STH) (determined from concentration of evolved H₂ gas measured under illumination of 100 mW cm⁻² with no applied potential as shown in Fig. 7a) vs irradiation time for Bilayer-2 NTs.

$\sim 19.88\%$ under 0.6 V bias) and the consequent polarization losses ($\sim 1.76\%$ at zero bias and $\sim 3\%$ under 0.6 V bias) to achieve high STH (at zero applied bias) and ABPE for bilayer-2 system configuration (Fig. 5c). Hence, it is critical to change the band edge levels in the bilayer 2 material configuration considered herein further which will offer improved light absorption and also superior band bending at the electrode/electrolyte interface aiding the facile transport of the excited carriers through the material. Such facile transport of carriers through the bilayer-2 material will offer lower recombination losses and superior PEC response with need of minimal or even zero applied bias, resulting in lower recombination and polarization losses. This strategy discussed herein can indeed lead to engineering of novel semiconductor materials for PEC process, which can be likely achieved by the introduction of suitable acceptor/donor levels in the band gap of the semiconductor material. These strategies can be indeed pursued in the near future.

Study of carrier lifetime

To understand the charge transport properties of the bilayer photoanode materials in detail, recombination kinetics of the

photo-generated carriers is studied by measuring the open circuit potential as a function of time under light OFF conditions. When the semiconductor material is illuminated with the solar light, the apparent Fermi level shifts to negative potential due to the accumulation of photo-generated electrons in the semiconductor material (under open circuit conditions) [30,81]. When the illumination is turned off, the accumulated electrons are discharged in the electrolyte solution as they are scavenged by the redox species in the electrolyte solution [30,81]. The recombination of photo-generated carriers is mainly responsible for the sharp decay of the photo-generated electrons [30,81]. The decay in the open circuit potential (V_{oc}) gives information about the rate of recombination of the photo-generated carriers in the semiconductor material [30,81]. The decay in V_{oc} as function of time is shown in Fig. 6a. The decay was calculated from the slope by considering different points in the corresponding rising and saturated segments of the curve, similar to earlier reports [30,67,81–86]. As seen in Fig. 6a, Bilayer-1 NTs (~ 8.4 mV s⁻¹) and Bilayer-2 NTs (~ 7.7 mV s⁻¹) exhibit slower V_{oc} decay rate than (Sn_{0.95}Nb_{0.05})O₂:N-600 NTs (~ 9.6 mV s⁻¹), suggesting lower recombination of photo-generated carriers

in the bilayer materials. On the other hand, Bilayer-3 NTs ($\sim 12.6 \text{ mV s}^{-1}$) has a much higher V_{oc} decay rate than $(\text{Sn}_{0.95}\text{Nb}_{0.05})\text{O}_2\text{:N-600}$ NTs, Bilayer-1 NTs and Bilayer-2 NTs, which can be due to the higher thickness of $(\text{Sn}_{0.95}\text{Nb}_{0.05})\text{O}_2\text{:N-600}$ NTs layer coated on WO_3 layer resulting in long transport distance to be traversed by the photo-generated carriers resulting in more recombination of the photo-generated carriers, which is similar to earlier reports [83,84]. The carrier lifetime (τ), which is the average time for which photo-generated carriers exist before recombining, is determined using the equation [29,84]:

$$\tau = -(k_B T/e)(dV_{oc}/dt)^{-1}$$

where, k_B is Boltzmann constant, T is the absolute temperature (299 K), e is electron charge. The variation of τ with V_{oc} , shown in Fig. 6b, shows significantly longer carrier lifetime for Bilayer-1 NTs and Bilayer-2 NTs with the highest lifetime seen for Bilayer-2 NTs than that of $(\text{Sn}_{0.95}\text{Nb}_{0.05})\text{O}_2\text{:N-600}$ NTs due to a relatively lower recombination rate of photo-generated carriers for the bilayer materials (as discussed before) (Fig. 6a).

However, lower carrier lifetime for Bilayer-3 NTs than the other materials considered in this study can be due to higher recombination kinetics of the photo-generated carriers due to the larger thickness of $(\text{Sn}_{0.95}\text{Nb}_{0.05})\text{O}_2\text{:N-600}$ NTs layer coated on WO_3 layer offering long transport distance to be covered by the photo-generated carriers, which is similar to earlier reports [83,84]. The largest carrier lifetime ($\sim 140 \text{ s}$) at (-0.2 V vs RHE) which is near zero bias and selected following the earlier reports in the literature [30,67,81–86]) obtained in this study for Bilayer-2 NTs plays an important role in achieving the superior photo-electrochemical activity, as seen in Fig. 5a. These results clearly suggest the beneficial role of the optimal bilayer structure, i.e., coupling of $(\text{Sn}_{0.95}\text{Nb}_{0.05})\text{O}_2\text{:N-600}$ NTs with WO_3 in increasing the carrier lifetime ~ 20 fold higher (at -0.2 V vs RHE) obtained for Bilayer-2 NTs compared to $(\text{Sn}_{0.95}\text{Nb}_{0.05})\text{O}_2\text{:N-600}$ NTs ($\sim 7 \text{ s}$ at -0.2 V vs RHE) and thus, minimizing the recombination of the photo-generated carriers. This is very important in the aim to achieve superior photo-electrochemical performance and thus, yield an efficient PEC water splitting process resulting in effective generation of hydrogen.

Photo-electrochemical stability of Bilayer-2 NTs

It is important that the semiconductor material exhibits excellent long term photo-electrochemical stability for achieving continuous, durable and efficient PEC water splitting. In order to demonstrate the durability and stability of the semiconductor material, chrono-amperometry (CA) test has been carried out for 24 h to study the long term photo-electrochemical stability of the optimal bilayer composite architecture, Bilayer-2 NTs under constant illumination in the electrolyte solution. The CA test is thus carried out in harsh operating conditions at a constant potential of $\sim 0.6 \text{ V (vs RHE)}$, similar to earlier reports [35,112,113]) in $0.5 \text{ M H}_2\text{SO}_4$ solution by illuminating the photoanode (100 mW cm^{-2}) for 24 h. The CA curve of Bilayer-2 NTs is shown in Fig. 7a. The very minimal loss in photocurrent density ($\sim 1\%$) is seen for Bilayer-2 NTs indicating the excellent long term photo-electrochemical stability of this composite bilayer system.

Inductively coupled plasma optical emission spectroscopy (ICP-OES) analysis conducted on the electrolyte solution, collected after CA test, did not show presence ($\sim 0 \text{ ppm}$) of Sn, Nb and W for Bilayer-2 NTs (see Table S2). This result essentially demonstrates the potential of the Bilayer-2 NTs system to display excellent photo-electrochemical stability in the electrolyte solution under illumination thus validating its long term operation in a PEC water splitting cell. The result thus confirms the stable and long term use of this system under actual field scale PEC operating conditions. The PEC stability study (under illumination) of bilayer-2 material in different pH environment along with a detailed assessment of the electronic properties of the bilayer system of different architectures and carrier lifetime studies will be planned in the future and reported in subsequent publications.

Measurement of evolved H_2 and O_2 gases under illumination for Bilayer-2 NTs

As mentioned earlier, it is important to achieve efficient hydrogen generation from PEC water splitting with utilization of only solar energy without any applied external potential. Hence, the optimal configuration of the bilayer composite photoanode of Bilayer-2 NTs was illuminated for 24 h without any application of external potential. The concentration of the resulting H_2 and O_2 gases evolved during the PEC water splitting process at the cathode and photoanode compartments, respectively, has been measured after each 1 h time interval. Also, the theoretical concentration of H_2 gas is calculated from the measured photocurrent by Faraday's law as [35,49]:

$$\text{No. of moles of H}_2 = \frac{Q}{2F} = \frac{It}{2F} = \frac{\int_0^t I \cdot dt}{2F}$$

where, I is the photocurrent density, t is time, F is the Faraday constant ($96,484.34 \text{ C mol}^{-1}$) and Q is the quantity of charge in coulomb. The concentration of evolved H_2 and O_2 gases, shown in Fig. 7b, shows the measured amount of evolved H_2 gas which is closer or comparable to the theoretical amount of H_2 , suggesting $\sim 100\%$ Faradaic efficiency. If the decomposition of water were to occur in a non-stoichiometric fashion, there will be change in concentration of either H^+ or OH^- ions. However, in this study, the ratio of concentration of generated H_2 and O_2 gases is ~ 2 , as seen in Fig. 7b and there was no change observed in the pH of the electrolyte solution (~ 0) before and after water the splitting reaction. This result thus, shows stoichiometric decomposition of water into H_2 and O_2 is achieved in the present study for Bilayer-2 NTs. The ensuing solar-to-hydrogen efficiency (STH) is determined from the measured concentration of H_2 gas for Bilayer-2 NTs using the equation [49,114–117]:

$$\text{STH} = \frac{\Delta G^\circ \times n_{\text{H}_2}}{P \times A} \times 100$$

where, n_{H_2} = H_2 evolution rate (mol sec^{-1}).

ΔG° = Gibbs free energy for generating 1 mol of H_2 from water ($237,130 \text{ J mol}^{-1}$).

P = Total incident power (W cm^{-2}).

A = Area irradiated by incident light (cm^2).

The plot of STH vs irradiation time is shown in Fig. 7c. At the end of 24 h, a minimal loss of (~1%) is seen in the STH for Bilayer-2 NTs indicating the excellent long term photo-electrochemical stability for continuous hydrogen generation from PEC water splitting under acidic conditions. It is noteworthy to mention herein that the STH of ~3.83% for Bilayer-2 NTs (with zero applied potential) achieved in the current study for the optimal bilayer composite configuration is the highest STH obtained so far compared to other semiconductor materials studied as photoanode and reported for PEC water splitting to the best of our knowledge. These include systems such as TiO₂, ZnO and Fe₂O₃ that have been studied to the best of our assessment of the widely reported literature to date [35,49,62–65]. Moreover, the efficiency achieved herein is also comparable to the efficiency achieved with artificial leaf based on the integration of three junction solar cells and optimized hydrogen- and oxygen-evolution catalysts [118]. The input power for Bilayer-2 NTs and thus, for H₂ production is ~100 mW cm⁻². The measured H₂ concentration is ~60 μmol/h/cm² (1.2 × 10⁻⁷ kg/h/cm²); (Fig. 7b). Thus, required input power for generation of 1 kg H₂ is ~833 kWh/kg (for 1 cm² area), which is higher than DOE target of <43 kWh/kg. Thus, albeit the electricity cost (~\$0.031/kWh) for the current system (\$25.83/kg) is ~20 fold higher than that of DOE target (~\$1.33/kg), it is still lower than other semiconductor materials (TiO₂, ZnO and Fe₂O₃) studied for PEC water splitting process reported in the literature thus far. There is clearly still much research needed but the bilayer system studied herein nevertheless, indeed holds promise on the grounds of recommendable PEC performance showing STH of ~3.83% (at zero applied bias) and ABPE of ~5.1% (at 0.6 V vs RHE) higher than other semiconductor materials (TiO₂, ZnO and Fe₂O₃) studied reported in the literature for PEC water splitting process.

As discussed earlier, light absorption losses, recombination losses and polarization losses mainly limit STH/ABPE and electricity cost for the bilayer system (Fig. 5c). As shown earlier, recombination losses decrease by a commendable ~12% for Bilayer-2 NTs under the applied bias of ~0.6 V (vs RHE) compared to the no bias condition, suggesting promise of the composite bilayer-2 system. Despite these losses, Bilayer-2 NTs show excellent PEC performance under applied bias with recommendable ABPE of ~5.1% (at ~0.6 V vs RHE) and STH of ~3.83% (under no bias). Hence, Bilayer-2 NTs bilayer system is indeed promising and further electronic structural modification of bilayer system by changing the band edge positions, which can be achieved by introduction of suitable acceptor/donor levels (in the band gap), will help in tailoring the band levels further. This will further help in lowering the above mentioned losses and hence, likely contribute to achieving higher STH (at zero applied bias) and superior ABPE (under minimal applied bias) while also lowering the electricity costs meeting and even exceeding the DOE targets. Additional research into this system and further overcoming the losses discussed earlier could also lead to additional improvements in the resultant STH efficiencies. The results of the studies described herein are therefore clearly transformational and serve towards fulfilling the goals of efficiently producing hydrogen by the direct utilization of solar energy in an environmentally friendly manner. Taken together, the results clearly represent a major milestone in solving the global energy demand with the generation of minimum greenhouse gas emissions.

Conclusions

The photoelectrochemical activity of the composite bilayer photoanode is studied in the present work with consideration of different thicknesses of (Sn_{0.95}Nb_{0.05})O₂:N-600. The work clearly demonstrates the potential of coupling WO₃ with (Sn_{0.95}Nb_{0.05})O₂:N-600, which offers excellent optoelectronic properties, improved charge transport and longer carrier lifetime with minimum recombination of photogenerated carriers (~20 fold higher carrier lifetime for Bilayer-2 NTs than (Sn_{0.95}Nb_{0.05})O₂:N-600). This results in excellent photo-electrochemical activity and STH of ~3.83% and ABPE of ~5.1% (at ~0.6 V vs RHE), along with negative onset potential for the optimal bilayer materials with the lowest (-0.55 V vs RHE) obtained for Bilayer-2 NTs. The superior light absorption properties along with significantly improved carrier density (~5.6 × 10²² cm⁻³) for Bilayer-2 NTs opens up a new territory for this material for different solar energy based applications. An excellent STH of ~3.83% (with no external potential applied) and ABPE of ~5.1% (at ~0.6 V vs RHE) is obtained for Bilayer-2 NTs, which is the highest reported so far compared to other photoanode materials like ZnO, Fe₂O₃ and TiO₂, to the best of our knowledge. Accordingly, the composite bilayer, Bilayer-2 NTs exhibited excellent long term photo-electrochemical stability with very minimal loss in photo-current density (~1%) in the acidic electrolyte solution under illumination. Hence, we believe that this work will be important for developing photoelectrochemically active and stable semiconductor materials for efficient and economic hydrogen generation from PEC water splitting.

Acknowledgments

Research in part supported by the National Science Foundation, CBET – Grant # 0933141 and CBET – Grant # 1511390. PNK acknowledges the Edward R. Weidlein Chair Professorship funds and the Center for Complex Engineered Multifunctional Materials (CCEMM), Swanson school of Engineering, University of Pittsburgh, for support of this research and also for procurement of the electrochemical equipment and facilities used in this research work.

Appendix A. Supplementary data

Supplementary data related to this article can be found at <https://doi.org/10.1016/j.ijhydene.2018.05.063>.

REFERENCES

- [1] Nowotny J, Bak T, Chu D, Fiechter S, Murch GE, Veziroglu TN. Sustainable practices: solar hydrogen fuel and education program on sustainable energy systems. *Int J Hydrogen Energy* 2014;39:4151–7.
- [2] Andrews J, Shabani B. The role of hydrogen in a global sustainable energy strategy. *Wiley Interdiscipl Rev Energy Environ* 2014;3:474–89.

- [3] Marchenko OV, Solomin SV. The future energy: hydrogen versus electricity. *Int J Hydrogen Energy* 2015;40:3801–5.
- [4] Nicoletti G, Arcuri N, Nicoletti G, Bruno R. A technical and environmental comparison between hydrogen and some fossil fuels. *Energy Convers Manag* 2015;89:205–13.
- [5] Peters GP, Andrew RM, Boden T, Canadell JG, Ciais P, Le Quere C, et al. The challenge to keep global warming below 2 °C. *Nat Clim Change* 2013;3:4–6.
- [6] Patel PP, Datta MK, Velikokhatnyi OI, Kuruba R, Damodaran K, Jampani P, et al. Noble metal-free bifunctional oxygen evolution and oxygen reduction acidic media electro-catalysts. *Sci Rep* 2016;6:28367.
- [7] Sharma S, Ghoshal SK. Hydrogen the future transportation fuel: from production to applications. *Renew Sustain Energy Rev* 2015;43:1151–8.
- [8] Turner JA. A realizable renewable energy future. *Science* 1999;285:687–9.
- [9] Turner JA. Sustainable hydrogen production. *Science* 2004;305:972–4.
- [10] Patel PP, Datta MK, Velikokhatnyi OI, Jampani P, Hong D, Poston JA, et al. Nanostructured robust cobalt metal alloy based anode electro-catalysts exhibiting remarkably high performance and durability for proton exchange membrane fuel cells. *J Mater Chem* 2015;3:14015–32.
- [11] Patel PP, Velikokhatnyi OI, Ghadge SD, Jampani PH, Datta MK, Hong D, et al. Highly active robust oxide solid solution electro-catalysts for oxygen reduction reaction for proton exchange membrane fuel cell and direct methanol fuel cell cathodes. *Int J Hydrogen Energy* 2017;42:24079–89.
- [12] Patel PP, Datta MK, Jampani PH, Hong D, Poston JA, Manivannan A, et al. High performance and durable nanostructured TiN supported Pt50–Ru50 anode catalyst for direct methanol fuel cell (DMFC). *J Power Sources* 2015;293:437–46.
- [13] Ghadge SD, Patel PP, Datta MK, Velikokhatnyi OI, Kuruba R, Shanthi PM, et al. Fluorine substituted (Mn, Ir)O₂:F high performance solid solution oxygen evolution reaction electro-catalysts for PEM water electrolysis. *RSC Adv* 2017;7:17311–24.
- [14] Patel PP, Hanumantha PJ, Datta MK, Velikokhatnyi OI, Hong D, Poston JA, et al. Cobalt based nanostructured alloys: versatile high performance robust hydrogen evolution reaction electro-catalysts for electrolytic and photo-electrochemical water splitting. *Int J Hydrogen Energy* 2017;42:17049–62.
- [15] Parker AR, Lawrence CR. Water capture by a desert beetle. *Nature* 2001;414:33–4.
- [16] Lewis NS, Nocera DG. Powering the planet: chemical challenges in solar energy utilization. *Proc Natl Acad Sci Unit States Am* 2006;103:15729–35.
- [17] Turner J, Sverdrup G, Mann MK, Maness PC, Kroposki B, Ghirardi M, et al. Renewable hydrogen production. *Int J Energy Res* 2008;32:379–407.
- [18] Winter C-J. Hydrogen energy—abundant, efficient, clean: a debate over the energy-system-of-change. *Int J Hydrogen Energy* 2009;34:S1–52.
- [19] Bard AJ, Fox MA. Artificial photosynthesis: solar splitting of water to hydrogen and oxygen. *Acc Chem Res* 1995;28:141–5.
- [20] Balat M, Balat M. Political, economic and environmental impacts of biomass-based hydrogen. *Int J Hydrogen Energy* 2009;34:3589–603.
- [21] Bak T, Nowotny J, Rekas M, Sorrell C. Photo-electrochemical hydrogen generation from water using solar energy. Materials-related aspects. *Int J Hydrogen Energy* 2002;27:991–1022.
- [22] Crabtree GW, Dresselhaus MS, Buchanan MV. The hydrogen economy. *Phys Today* 2004;57:39–44.
- [23] Zou Z, Ye J, Sayama K, Arakawa H. Direct splitting of water under visible light irradiation with an oxide semiconductor photocatalyst. *Nature* 2001;414:625–7.
- [24] Cipriani G, Di Dio V, Genduso F, La Cascia D, Liga R, Miceli R, et al. Perspective on hydrogen energy carrier and its automotive applications. *Int J Hydrogen Energy* 2014;39:8482–94.
- [25] Chen X, Shen S, Guo L, Mao SS. Semiconductor-based photocatalytic hydrogen generation. *Chem Rev* 2010;110:6503–70.
- [26] Walter MG, Warren EL, McKone JR, Boettcher SW, Mi Q, Santori EA, et al. Solar water splitting cells. *Chem Rev* 2010;110:6446–73.
- [27] Patel PP, Velikokhatnyi OI, Ghadge SD, Hanumantha PJ, Datta MK, Kuruba R, et al. Electrochemically active and robust cobalt doped copper phosphosulfide electro-catalysts for hydrogen evolution reaction in electrolytic and photoelectrochemical water splitting. *Int J Hydrogen Energy* 2018;43:7855–71.
- [28] Peng X, He C, Fan X, Liu Q, Zhang J, Wang H. Photovoltaic devices in hydrogen production. *Int J Hydrogen Energy* 2014;39:14166–71.
- [29] Fujishima A. Electrochemical photolysis of water at a semiconductor electrode. *Nature* 1972;238:37–8.
- [30] Kushwaha A, Aslam M. ZnS shielded ZnO nanowire photoanodes for efficient water splitting. *Electrochim Acta* 2014;130:222–31.
- [31] Kronawitter CX, Vayssieres L, Shen S, Guo L, Wheeler DA, Zhang JZ, et al. A perspective on solar-driven water splitting with all-oxide hetero-nanostructures. *Energy Environ Sci* 2011;4:3889–99.
- [32] Chen HM, Chen CK, Liu R-S, Zhang L, Zhang J, Wilkinson DP. Nano-architecture and material designs for water splitting photoelectrodes. *Chem Soc Rev* 2012;41:5654–71.
- [33] Osterloh FE. Inorganic nanostructures for photoelectrochemical and photocatalytic water splitting. *Chem Soc Rev* 2013;42:2294–320.
- [34] Zhang X, Liu Y, Kang Z. 3D branched ZnO nanowire arrays decorated with plasmonic Au nanoparticles for high-performance photoelectrochemical water splitting. *ACS Appl Mater Interfaces* 2014;6:4480–9.
- [35] Patel PP, Hanumantha PJ, Velikokhatnyi OI, Datta MK, Hong D, Gattu B, et al. Nitrogen and cobalt co-doped zinc oxide nanowires – viable photoanodes for hydrogen generation via photoelectrochemical water splitting. *J Power Sources* 2015;299:11–24.
- [36] Ni M, Leung MK, Leung DY, Sumathy K. A review and recent developments in photocatalytic water-splitting using TiO₂ for hydrogen production. *Renew Sustain Energy Rev* 2007;11:401–25.
- [37] Yang X, Wolcott A, Wang G, Sobo A, Fitzmorris RC, Qian F, et al. Nitrogen-doped ZnO nanowire arrays for photoelectrochemical water splitting. *Nano Lett* 2009;9:2331–6.
- [38] Tacca A, Meda L, Marra G, Savoini A, Caramori S, Cristino V, et al. Photoanodes based on nanostructured WO₃ for water splitting. *ChemPhysChem* 2012;13:3025–34.
- [39] Kitano M, Matsuoka M, Ueshima M, Anpo M. Recent developments in titanium oxide-based photocatalysts. *Appl Catal A Gen* 2007;325:1–14.
- [40] Sang L, Lin J, Zhao Y. Preparation of carbon dots/TiO₂ electrodes and their photoelectrochemical activities for water splitting. *Int J Hydrogen Energy* 2017;42:12122–32.
- [41] Sivula K, Le Formal F, Grätzel M. Solar water splitting: progress using hematite (α -Fe₂O₃) photoelectrodes. *ChemSusChem* 2011;4:432–49.
- [42] Osterloh FE, Parkinson BA. Recent developments in solar water-splitting photocatalysis. *MRS Bull* 2011;36:17–22.

- [43] Mayer MA, Yu KM, Speaks DT, Denlinger JD, Reichertz LA, Beeman JW, et al. Band gap engineering of oxide photoelectrodes: characterization of ZnO 1-xSe x. *J Phys Chem C* 2012;116:15281–9.
- [44] Govatsi K, Seferlis A, Neophytides S, Yannopoulos S. Influence of the morphology of ZnO nanowires on the photoelectrochemical water splitting efficiency. *Int J Hydrogen Energy* 2018;43:4866–79.
- [45] Feng W, Lin L, Li H, Chi B, Pu J, Li J. Hydrogenated TiO₂/ZnO heterojunction nanorod arrays with enhanced performance for photoelectrochemical water splitting. *Int J Hydrogen Energy* 2017;42:3938–46.
- [46] Datta MK, Kadakia K, Velikokhatnyi OI, Jampani PH, Chung SJ, Poston JA, et al. High performance robust F-doped tin oxide based oxygen evolution electro-catalysts for PEM based water electrolysis. *J Mater Chem A* 2013;1:4026–37.
- [47] Tamaki Y, Hara K, Katoh R, Tachiya M, Furube A. Femtosecond visible-to-IR spectroscopy of TiO₂ nanocrystalline films: elucidation of the electron mobility before deep trapping†. *J Phys Chem C* 2009;113:11741–6.
- [48] Ramasamy E, Lee J. Ordered mesoporous SnO₂-based photoanodes for high-performance dye-sensitized solar cells. *J Phys Chem C* 2010;114:22032–7.
- [49] Patel PP, Hanumantha PJ, Velikokhatnyi OI, Datta MK, Gattu B, Poston JA, et al. Vertically aligned nitrogen doped (Sn,Nb)O₂ nanotubes – robust photoanodes for hydrogen generation by photoelectrochemical water splitting. *Mater Sci Eng B* 2016;208:1–14.
- [50] Wang Y, Wang Q, Zhan X, Wang F, Safdar M, He J. Visible light driven type II heterostructures and their enhanced photocatalysis properties: a review. *Nanoscale* 2013;5:8326–39.
- [51] Wang Y, Brezesinski T, Antonietti M, Smarsly B. Ordered mesoporous Sb-, Nb-, and Ta-doped SnO₂ thin films with adjustable doping levels and high electrical conductivity. *ACS Nano* 2009;3:1373–8.
- [52] Gokulakrishnan V, Parthiban S, Jeganathan K, Ramamurthi K. Investigations on the structural, optical and electrical properties of Nb-doped SnO₂ thin films. *J Mater Sci* 2011;46:5553–8.
- [53] Stefić M, Cornuz M, Mathews N, Hisatomi T, Mhaisalkar S, Grätzel M. Transparent, conducting Nb: SnO₂ for host-guest photoelectrochemistry. *Nano Lett* 2012;12:5431–5.
- [54] Turgut G, Keskenler E, Aydın S, Yılmaz M, Doğan S, Düzgün B. An investigation of the Nb doping effect on structural, morphological, electrical and optical properties of spray deposited F doped SnO₂ films. *Phys Scripta* 2013;87:035602.
- [55] Shamoto S-i, Nakano T, Nozue Y, Kajitani T. Substitution effects on ferromagnetic Mott insulator Lu₂V₂O₇. *J Phys Chem Solid* 2002;63:1047–50.
- [56] Katiyar R, Dawson P, Hargreave M, Wilkinson G. Dynamics of the rutile structure. III. Lattice dynamics, infrared and Raman spectra of SnO₂. *J Phys C Solid State Phys* 1971;4:2421–31.
- [57] Maeda K. (Oxy)nitrides with d⁰-electronic configuration as photocatalysts and photoanodes that operate under a wide range of visible light for overall water splitting. *Phys Chem Chem Phys* 2013;15:10537–48.
- [58] Asahi R, Morikawa T, Ohwaki T, Aoki K, Taga Y. Visible-light photocatalysis in nitrogen-doped titanium oxides. *Science* 2001;293:269–71.
- [59] Burda C, Lou Y, Chen X, Samia ACS, Stout J, Gole JL. Enhanced nitrogen doping in TiO₂ nanoparticles. *Nano Lett* 2003;3:1049–51.
- [60] Beranek R, Neumann B, Sakthivel S, Janczarek M, Dittrich T, Tributsch H, et al. Exploring the electronic structure of nitrogen-modified TiO₂ photocatalysts through photocurrent and surface photovoltage studies. *Chem Phys* 2007;339:11–9.
- [61] Hoang S, Guo S, Hahn NT, Bard AJ, Mullins CB. Visible light driven photoelectrochemical water oxidation on nitrogen-modified TiO₂ nanowires. *Nano Lett* 2011;12:26–32.
- [62] Cho IS, Chen Z, Forman AJ, Kim DR, Rao PM, Jaramillo TF, et al. Branched TiO₂ nanorods for photoelectrochemical hydrogen production. *Nano Lett* 2011;11:4978–84.
- [63] Wang G, Wang H, Ling Y, Tang Y, Yang X, Fitzmorris RC, et al. Hydrogen-treated TiO₂ nanowire arrays for photoelectrochemical water splitting. *Nano Lett* 2011;11:3026–33.
- [64] Dotan H, Sivula K, Grätzel M, Rothschild A, Warren SC. Probing the photoelectrochemical properties of hematite ([small alpha]-Fe₂O₃) electrodes using hydrogen peroxide as a hole scavenger. *Energy Environ Sci* 2011;4:958–64.
- [65] Liu Q, Ding D, Ning C, Wang X. Black Ni-doped TiO₂ photoanodes for high-efficiency photoelectrochemical water-splitting. *Int J Hydrogen Energy* 2015;40:2107–14.
- [66] Sasikala R, Shirole A, Sudarsan V, Sakuntala T, Sudakar C, Naik R, et al. Highly dispersed phase of SnO₂ on TiO₂ nanoparticles synthesized by polyol-mediated route: photocatalytic activity for hydrogen generation. *Int J Hydrogen Energy* 2009;34:3621–30.
- [67] Hernández S, Cauda V, Chiodoni A, Dallorto S, Sacco A, Hidalgo D, et al. Optimization of 1D ZnO@TiO₂ core-shell nanostructures for enhanced photoelectrochemical water splitting under solar light illumination. *ACS Appl Mater Interfaces* 2014;6:12153–67.
- [68] Schrier J, Demchenko DO, Wang L-W, Alivisatos AP. Optical properties of ZnO/ZnS and ZnO/ZnTe heterostructures for photovoltaic applications. *Nano Lett* 2007;7:2377–82.
- [69] Law M, Greene LE, Johnson JC, Saykally R, Yang P. Nanowire dye-sensitized solar cells. *Nat Mater* 2005;4:455–9.
- [70] Mai L, Tian X, Xu X, Chang L, Xu L. Nanowire electrodes for electrochemical energy storage devices. *Chem Rev* 2014;114:11828–62.
- [71] Cole B, Marsen B, Miller E, Yan Y, To B, Jones K, et al. Evaluation of nitrogen doping of tungsten oxide for photoelectrochemical water splitting. *J Phys Chem C* 2008;112:5213–20.
- [72] Rodríguez-Pérez M, Chacón C, Palacios-González E, Rodríguez-Gattorno G, Oskam G. Photoelectrochemical water oxidation at electrophoretically deposited WO₃ films as a function of crystal structure and morphology. *Electrochim Acta* 2014;140:320–31.
- [73] Prabhu S, Cindrella L, Kwon OJ, Mohanraju K. Green synthesis of rGO-WO₃ composite and its efficient photoelectrochemical water splitting. *Int J Hydrogen Energy* 2017;42:29791–6.
- [74] Yu S, Ling Y, Zhang J, Qin F, Zhang Z. Efficient photoelectrochemical water splitting and impedance analysis of WO₃-x nanoflake electrodes. *Int J Hydrogen Energy* 2017;42:20879–87.
- [75] Sadakane M, Sasaki K, Kunioku H, Ohtani B, Abe R, Ueda W. Preparation of 3-D ordered macroporous tungsten oxides and nano-crystalline particulate tungsten oxides using a colloidal crystal template method, and their structural characterization and application as photocatalysts under visible light irradiation. *J Mater Chem* 2010;20:1811–8.
- [76] Deki S, Iizuka S, Horie A, Mizuhata M, Kajinami A. Liquid-phase infiltration (LPI) process for the fabrication of highly nano-ordered materials. *Chem Mater* 2004;16:1747–50.
- [77] Lee J-H, Leu I-C, Hsu M-C, Chung Y-W, Hon M-H. Fabrication of aligned TiO₂ one-dimensional nanostructured arrays using a one-step templating solution approach. *J Phys Chem B* 2005;109:13056–9.

- [78] Desai UV, Xu C, Wu J, Gao D. Hybrid TiO₂–SnO₂ nanotube arrays for dye-sensitized solar cells. *J Phys Chem C* 2013;117:3232–9.
- [79] Minggu LJ, Wan Daud WR, Kassim MB. An overview of photocells and photoreactors for photoelectrochemical water splitting. *Int J Hydrogen Energy* 2010;35:5233–44.
- [80] Patel PP, Jampani PH, Datta MK, Velikokhatnyi OI, Hong D, Poston JA, et al. WO₃ based solid solution oxide – promising proton exchange membrane fuel cell anode electrocatalyst. *J Mater Chem* 2015;3:18296–309.
- [81] Kang Q, Cao J, Zhang Y, Liu L, Xu H, Ye J. Reduced TiO₂ nanotube arrays for photoelectrochemical water splitting. *J Mater Chem* 2013;1:5766–74.
- [82] Han HS, Shin S, Noh JH, Cho IS, Hong KS. Heterojunction Fe₂O₃–SnO₂ nanostructured photoanode for efficient photoelectrochemical water splitting. *JOM* 2014;66:664–9.
- [83] Lai CW, Sreekantan S. Incorporation of WO₃ species into TiO₂ nanotubes via wet impregnation and their water-splitting performance. *Electrochim Acta* 2013;87:294–302.
- [84] Liu Q, Lu H, Shi Z, Wu F, Guo J, Deng K, et al. 2D ZnIn₂S₄ nanosheet/1D TiO₂ nanorod heterostructure arrays for improved photoelectrochemical water splitting. *ACS Appl Mater Interfaces* 2014;6:17200–7.
- [85] Zaban A, Greenshtein M, Bisquert J. Determination of the electron lifetime in nanocrystalline dye solar cells by open-circuit voltage decay measurements. *ChemPhysChem* 2003;4:859–64.
- [86] Zhang K, Shi X-J, Kim JK, Park JH. Photoelectrochemical cells with tungsten trioxide/Mo-doped BiVO₄ bilayers. *Phys Chem Chem Phys* 2012;14:11119–24.
- [87] Li Y, Takata T, Cha D, Takanabe K, Minegishi T, Kubota J, et al. Vertically aligned Ta₃N₅ nanorod arrays for solar-driven photoelectrochemical water splitting. *Adv Mater* 2013;25:125–31.
- [88] Higashi M, Domen K, Abe R. Fabrication of efficient TaON and Ta₃N₅ photoanodes for water splitting under visible light irradiation. *Energy Environ Sci* 2011;4:4138–47.
- [89] AlOtaibi B, Nguyen HPT, Zhao S, Kibria MG, Fan S, Mi Z. Highly stable photoelectrochemical water splitting and hydrogen generation using a double-band InGaN/GaN core/shell nanowire photoanode. *Nano Lett* 2013;13:4356–61.
- [90] Choi WK, Jung HJ, Koh SK. Chemical shifts and optical properties of tin oxide films grown by a reactive ion assisted deposition. *J Vac Sci Technol A* 1996;14:359–66.
- [91] Sathish M, Viswanathan B, Viswanath RP, Gopinath CS. Synthesis, characterization, electronic structure, and photocatalytic activity of nitrogen-doped TiO₂ nanocatalyst. *Chem Mater* 2005;17:6349–53.
- [92] Ohnishi R, Katayama M, Takanabe K, Kubota J, Domen K. Niobium-based catalysts prepared by reactive radio-frequency magnetron sputtering and arc plasma methods as non-noble metal cathode catalysts for polymer electrolyte fuel cells. *Electrochim Acta* 2010;55:5393–400.
- [93] Himmerlich M, Koufaki M, Ecke G, Mauder C, Cimalla V, Schaefer JA, et al. Effect of annealing on the properties of Indium–Tin–oxynitride films as ohmic contacts for GaN-based optoelectronic devices. *ACS Appl Mater Interfaces* 2009;1:1451–6.
- [94] Sarma DD, Rao CNR. XPS studies of oxides of second- and third-row transition metals including rare earths. *J Electron Spectrosc Relat Phenom* 1980;20:25–45.
- [95] Jouve J, Belkacem Y, Severac C. X-ray photoelectron spectroscopy study of phosphorus incorporation in anodic oxide films on niobium. *Thin Solid Films* 1986;139:67–75.
- [96] Chen Z, Cummins D, Reinecke BN, Clark E, Sunkara MK, Jaramillo TF. Core–shell MoO₃–MoS₂ nanowires for hydrogen evolution: a functional design for electrocatalytic materials. *Nano Lett* 2011;11:4168–75.
- [97] Zhou J, Fang H, Maley J, Ko J, Murphy M, Chu Y, et al. An X-ray absorption, photoemission, and Raman study of the interaction between SnO₂ nanoparticle and carbon nanotube. *J Phys Chem C* 2009;113:6114–7.
- [98] Xie S, Lu X, Zhai T, Li W, Yu M, Liang C, et al. Enhanced photoactivity and stability of carbon and nitrogen co-treated ZnO nanorod arrays for photoelectrochemical water splitting. *J Mater Chem* 2012;22:14272–5.
- [99] Zheng Y-Z, Ding H, Tao X, Chen J-F. Investigation of iodine dopant amount effects on dye-sensitized hierarchically structured ZnO solar cells. *Mater Res Bull* 2014;55:182–9.
- [100] Wang G, Ling Y, Li Y. Oxygen-deficient metal oxide nanostructures for photoelectrochemical water oxidation and other applications. *Nanoscale* 2012;4:6682–91.
- [101] Qiu Y, Yan K, Deng H, Yang S. Secondary branching and nitrogen doping of ZnO nanotetrapods: building a highly active network for photoelectrochemical water splitting. *Nano Lett* 2011;12:407–13.
- [102] Bolts JM, Wrighton MS. Correlation of photocurrent-voltage curves with flat-band potential for stable photoelectrodes for the photoelectrolysis of water. *J Phys Chem* 1976;80:2641–5.
- [103] Yang C, Wang Z, Lin T, Yin H, Lü X, Wan D, et al. Core-shell nanostructured “Black” rutile titania as excellent catalyst for hydrogen production enhanced by sulfur doping. *J Am Chem Soc* 2013;135:17831–8.
- [104] Cui H, Zhao W, Yang C, Yin H, Lin T, Shan Y, et al. Black TiO₂ nanotube arrays for high-efficiency photoelectrochemical water-splitting. *J Mater Chem A* 2014;2:8612–6.
- [105] Li W, Li J, Wang X, Ma J, Chen Q. Photoelectrochemical and physical properties of WO₃ films obtained by the polymeric precursor method. *Int J Hydrogen Energy* 2010;35:13137–45.
- [106] Yagi M, Maruyama S, Sone K, Nagai K, Norimatsu T. Preparation and photoelectrocatalytic activity of a nanostructured WO₃ platelet film. *J Solid State Chem* 2008;181:175–82.
- [107] Wang G, Yang X, Qian F, Zhang JZ, Li Y. Double-sided CdS and CdSe quantum dot co-sensitized ZnO nanowire arrays for photoelectrochemical hydrogen generation. *Nano Lett* 2010;10:1088–92.
- [108] Kwak IH, Im HS, Jang DM, Kim YW, Park K, Lim YR, et al. CoSe₂ and NiSe₂ nanocrystals as superior bifunctional catalysts for electrochemical and photoelectrochemical water splitting. *ACS Appl Mater Interfaces* 2016;8:5327–34.
- [109] Su F, Wang T, Lv R, Zhang J, Zhang P, Lu J, et al. Dendritic Au/TiO₂ nanorod arrays for visible-light driven photoelectrochemical water splitting. *Nanoscale* 2013;5:9001–9.
- [110] Yang Y, Li X-j, Chen J-t, Wang L-y. Effect of doping mode on the photocatalytic activities of Mo/TiO₂. *J Photochem Photobiol A Chem* 2004;163:517–22.
- [111] Chen M, Blankenship RE. Expanding the solar spectrum used by photosynthesis. *Trends Plant Sci* 2011;16:427–31.
- [112] Pilli SK, Furtak TE, Brown LD, Deutsch TG, Turner JA, Herring AM. Cobalt-phosphate (Co-Pi) catalyst modified Mo-doped BiVO₄ photoelectrodes for solar water oxidation. *Energy Environ Sci* 2011;4:5028–34.
- [113] Pilli SK, Deutsch TG, Furtak TE, Turner JA, Brown LD, Herring AM. Light induced water oxidation on cobalt-phosphate (Co-Pi) catalyst modified semi-transparent, porous SiO₂–BiVO₄ electrodes. *Phys Chem Chem Phys* 2012;14:7032–9.
- [114] Bolton JR. Solar photoproduction of hydrogen: a review. *Sol Energy* 1996;57:37–50.
- [115] Liao C-H, Huang C-W, Wu J. Hydrogen production from semiconductor-based photocatalysis via water splitting. *Catalysts* 2012;2:490–516.

- [116] Chen Z, Jaramillo TF, Deutsch TG, Kleiman-Shwarsstein A, Forman AJ, Gaillard N, et al. Accelerating materials development for photoelectrochemical hydrogen production: standards for methods, definitions, and reporting protocols. *J Mater Res* 2010;25:3–16.
- [117] Coridan RH, Nielander AC, Francis SA, McDowell MT, Dix V, Chatman SM, et al. Methods for comparing the performance of energy-conversion systems for use in solar fuels and solar electricity generation. *Energy Environ Sci* 2015;8:2886–901.
- [118] Nocera DG. The artificial leaf. *Acc Chem Res* 2012;45:767–76.